



**HAL**  
open science

# Simulation of Mixture Flows: Pollution Spreading and Avalanches

Caterina Calgaro, Emmanuel Creusé, Thierry Goudon

► **To cite this version:**

Caterina Calgaro, Emmanuel Creusé, Thierry Goudon. Simulation of Mixture Flows: Pollution Spreading and Avalanches. 2012. hal-00732112v1

**HAL Id: hal-00732112**

**<https://hal.science/hal-00732112v1>**

Preprint submitted on 14 Sep 2012 (v1), last revised 23 Oct 2014 (v2)

**HAL** is a multi-disciplinary open access archive for the deposit and dissemination of scientific research documents, whether they are published or not. The documents may come from teaching and research institutions in France or abroad, or from public or private research centers.

L'archive ouverte pluridisciplinaire **HAL**, est destinée au dépôt et à la diffusion de documents scientifiques de niveau recherche, publiés ou non, émanant des établissements d'enseignement et de recherche français ou étrangers, des laboratoires publics ou privés.

# Simulation of Mixture Flows : Pollution Spreading and Avalanches

Caterina CALGARO \*    Emmanuel CREUSÉ \*    Thierry GOUDON †

September 13, 2012

## Abstract

We are concerned with the numerical simulation of certain multi-fluids flows, which in particular arises in the modeling of pollutant spreading and powder-snow avalanches. The behavior of the mixture is described through a single mass density and a velocity field, with an unusual constraint that relates the divergence of the velocity to derivatives of the density. We propose a numerical scheme based on a hybrid Finite Volume/Finite Element method. This approach is validated by comparison to analytical solutions and experimental data. The scheme works on unstructured meshes and it can be advantageously coupled to mesh refinements strategies in order to follow fronts of high density variation. We pay a specific attention to the behavior with respect to the leading coefficients that characterize the flow: the Froude and Reynolds numbers.

**Keywords :** Variable density flows. Mixture flows. Finite Volume method. Finite Element method. Unstructured meshes. Particulate flows and hydrodynamic regimes.

## Introduction

We are concerned with systems of PDEs describing the evolution of mixture flows. The fluid is described by the density  $\rho(t, x)$ , depending on time  $t \geq 0$  and space  $x \in \Omega \subset \mathbb{R}^N$ , and the velocity

---

\*Université Lille 1 - Laboratoire Paul Painlevé and E.P.I. SIMPAF - INRIA Lille Nord Europe, Cité scientifique, 59655 Villeneuve d'Ascq Cedex, France. [caterina.calgaro@math.univ-lille1.fr](mailto:caterina.calgaro@math.univ-lille1.fr), [emmanuel.creuse@math.univ-lille1.fr](mailto:emmanuel.creuse@math.univ-lille1.fr)

†E.P.I. COFFEE - INRIA Sophia Antipolis Méditerranée, 2004, route des Lucioles - BP 93, 06902 Sophia Antipolis Cedex & Labo. J. A. Dieudonné, CNRS-Université Nice Sophia Antipolis, UMR 7351, Parc Valrose 06108 Nice cedex 02, France. [thierry.goudon@inria.fr](mailto:thierry.goudon@inria.fr)

field  $u(t, x) \in \mathbb{R}^N$ . These quantities obey mass and momentum conservation, respectively, which read

$$\partial_t \rho + \nabla_x \cdot (\rho u) = 0, \quad (1)$$

and

$$\partial_t(\rho u) + \text{Div}_x(\rho u \otimes u) + \nabla_x p = \rho g + \text{Div}_x(\mu \mathbb{D}(u)) \quad (2)$$

with  $\mathbb{D}(u) = (\nabla_x u + \nabla_x u^T)$ . In (2),  $g$  stands for the gravity acceleration (but it can include further external forces), while  $\mu$  represents the dynamic viscosity of the fluid. This positive quantity might depend on the density  $\rho$  as we shall detail below. The originality of the modeling of mixtures relies on the definition of the pressure  $p$ . It is associated to the non-standard constraint

$$\nabla_x \cdot u = -\nabla_x \cdot (\kappa \nabla_x \ln(\rho)) \quad (3)$$

where  $\kappa$  is a positive coefficient. Of course, when  $\kappa = 0$  the system (1)–(3) is nothing but the usual Incompressible Navier–Stokes system. In this specific case,  $\nabla_x \cdot u = 0$ , the density remains constant along the characteristic curves  $(t, x) \mapsto X(t, x)$  of the flow:

$$\frac{d}{dt} [\rho(t, X(t, x))] = 0, \quad \frac{d}{dt} X(t, x) = u(t, X(t, x)), \quad X(0, x) = x$$

(as long as the definition of  $X$  makes sense). Accordingly, when the fluid is initially homogeneous, it remains homogeneous for ever. Dealing with non-homogeneous flows, the system (1)–(2) with  $\nabla_x \cdot u = 0$  couples equations of different types and it presents specific difficulties, both for mathematical analysis and numerical simulation. For instance, a fine analysis of the well-posedness issues can be found in [17, 19] and for further results and comments we refer to [40, Chapter 2]. Similarly, the numerical treatment is by no way a mere adaptation of the homogeneous case, see [13, 14] and the references therein. In this paper, we shall consider the case  $\kappa > 0$  and we wish to construct numerical methods able to handle this non-standard coupling.

The Fick law (3) relating the divergence of the velocity field to derivatives of the density has been introduced in [34, 38] and it has been further developed in [10, 30, 37, 48] for modeling flows where species (like salt or pollutant) are dissolved in a compressible or incompressible fluid. The mixture is regarded as an averaged continuum, described by a single density and velocity. Therefore, the density  $\rho$  is naturally highly non homogeneous, and the constitutive law (3) accounts for diffusion effects between the constituents of the mixture. It is worth pointing out that the model has been independently discussed as a correction to the standard fluid mechanics, even for single-phase flows [8, 11] (and for analysis reasonings that bring out remarkable mathematical structures of the corrected system, see [29]). In this work, we are particularly interested in the application of the model to reproduce powder–snow avalanches, as it has been proposed in [21, 24, 25]. Questions of existence and uniqueness of strong solutions are investigated in [6, 38, 50, 51], while the theory of weak solutions has been studied in [5, Chapter 3, Section 4]. The analysis has been completed recently in [12] by using energy estimates available when a specific relation holds between the

viscosity  $\mu$  and the coefficient  $\kappa$  (see below), and in [35] where the numerical analysis viewpoint is developed from a Finite Element approximation. It is worth mentioning that (1)–(2) completed with the constraint (3) shares many aspects with low Mach models which arise in combustion theory. In low Mach models the logarithm in (3) is replaced by another function of the density. We refer to [41, Section 8.8] for a sketch of analysis on weak solutions and to [1, 2] for further details. We shall go back to these questions elsewhere; here we focus on the difficulties introduced by the constraint (3).

In section 1 we review the basis of the derivation of the system (1)–(3) when describing mixture flows. This discussion is completed by an Appendix where we detail how the constitutive law can be derived from the Eulerian–Lagrangian modeling of particulate flows, in a certain hydrodynamic regime. In Section 1.2 we clarify the fact that different formulations of the problem can be naturally used and we present a hierarchy of models with gradual difficulties for numerics — and certainly for mathematical analysis too. Section 2 is mainly devoted to the numerical simulation of avalanche phenomena. First, we detail in Section 2.1 the principles of the numerical method we propose to solve the system. A hybrid scheme is introduced, which combines a Finite Volume method for solving the mass conservation equation to a Finite Element method for solving the momentum conservation equation and the constraint. This strategy is directly inspired from our works [14, 13] on incompressible flows. We point out that the scheme works on unstructured meshes and, thus it is well adapted to incorporate mesh refinement procedures. In turn, the scheme is quite efficient in capturing displacements of fronts, characterized by high variation of the density, a typical feature of powder–snow avalanches and pollutant dispersion. In Section 2.2, we check through numerical experiments and direct comparison with analytical solutions the accuracy properties of the scheme. Section 2.3 is concerned with the simulation of realistic avalanche phenomena, and we can compare the numerical tests to experimental data. It turns out that the Froude and the Reynolds numbers are the key parameters that govern the flow, and grade the numerical difficulty. Hence, we pay a specific attention to the investigation of the role of these parameters, based on numerical grounds. Finally, in Section 2.4, we turn to the simulation of an avalanche bumping into a wall.

## 1 Modeling of Mixtures

In this Section, we review various aspects of the derivation of the system (1)–(3). To this end, let us introduce a few notation. We assume that the mixture is made of a disperse phase interacting with a dense phase, but we shall adopt an averaged description of the flow. The two fluids that constitute the mixture are characterized by their reference mass density: we denote  $\bar{\rho}_f$  the density of the dense phase and  $\bar{\rho}_d$  the density of the dilute phase. We also need the velocity field of each constituent:  $u_f(t, x)$  and  $u_d(t, x)$ , respectively. We define the volume fraction of the disperse phase  $0 \leq \phi(t, x) \leq 1$ :

$$\phi(t, x) = \lim_{r \rightarrow 0} \frac{\text{Volume occupied at time } t \text{ by the disperse phase in } B(x, r)}{|B(x, r)|}.$$

Therefore, assuming that each phase is incompressible and keeps a constant mass density, the density of the mixture is defined by

$$\rho(t, x) = \underbrace{\bar{\rho}_f(1 - \phi(t, x))}_{:=\rho_f(t, x)} + \underbrace{\bar{\rho}_d\phi(t, x)}_{:=\rho_d(t, x)} = \bar{\rho}_f + (\bar{\rho}_d - \bar{\rho}_f)\phi(t, x).$$

We can write the mass conservation for the two phases

$$\partial_t \rho_f + \nabla_x \cdot (\rho_f u_f) = 0 = \partial_t \rho_d + \nabla_x \cdot (\rho_d u_d).$$

Accordingly we obtain

$$\partial_t \rho + \nabla_x \cdot (\rho u) = 0 \tag{4}$$

where

$$\rho u(t, x) = (\rho_f u_f + \rho_d u_d)(t, x),$$

defines the *mean mass velocity* (or barycentric velocity)  $u(t, x)$ . Note that, even if the two constituents are incompressible,  $u$  is not divergence free, by contrast to the *mean volume velocity*

$$v(t, x) = (1 - \phi(t, x))u_f(t, x) + \phi(t, x)u_d(t, x).$$

Indeed, the velocity field  $v$  is solenoidal because

$$\begin{aligned} \partial_t \left( \frac{\rho_f}{\bar{\rho}_f} + \frac{\rho_d}{\bar{\rho}_d} \right) &= \partial_t (1 - \phi + \phi) = 0 \\ &= -\nabla_x \cdot \left( \frac{\rho_f u_f}{\bar{\rho}_f} + \frac{\rho_d u_d}{\bar{\rho}_d} \right) = -\nabla_x \cdot v = 0. \end{aligned}$$

Next, we write the usual momentum equation for  $\rho u$ , that is

$$\partial_t(\rho u) + \text{Div}_x(\rho u \otimes u) + \nabla_x p = \rho g + \text{Div}_x(\mu \mathbb{D}(u))$$

with  $\mathbb{D}(u) = (\nabla_x u + \nabla_x u^T)$ . The definition of the pressure  $p$  comes from a constitutive relation which postulates a Fick law between  $u$ ,  $v$  and  $\rho$ .

## 1.1 The Kazhigov–Smagulov Model

According to Kazhikov and Smagulov [38] we set

$$u = v - \kappa \nabla_x \ln(\rho),$$

for some constant  $\kappa > 0$ . This Fick's law describes the diffusive fluxes of one fluid into the other [37, 48]. Clearly, this relation yields (3). In [30], it is found convenient to derive the Kazhikov–Smagulov relation from a similar relation for the fields associated to the dense phase, namely

$$u_f = u - \kappa \nabla_x \ln(\rho_f / \rho).$$

Here, we point out another relation, involving the evolution of the volume fraction.

**Lemma 1** *The following assertions are equivalent:*

*i) There exists  $\kappa > 0$  and a solenoidal field  $v$  such that  $u = v - \kappa \nabla_x \ln(\rho)$ ,*

*ii) There exists  $\tilde{\kappa} > 0$  such that the volume fraction  $\phi$  satisfies the convection–diffusion equation*

$$\partial_t \phi + \nabla_x \cdot (\phi u) = \nabla_x \cdot (\tilde{\kappa} \nabla_x \ln(\bar{\rho}_f + (\bar{\rho}_d - \bar{\rho}_f)\phi)).$$

**Proof.** We rewrite the mass conservation (4) as follows

$$\begin{aligned} \partial_t(\bar{\rho}_f + (\bar{\rho}_d - \bar{\rho}_f)\phi) + \nabla_x \cdot ((\bar{\rho}_f + (\bar{\rho}_d - \bar{\rho}_f)\phi)u) &= 0 \\ &= (\bar{\rho}_d - \bar{\rho}_f)(\partial_t \phi + \nabla_x \cdot (\phi u)) + \bar{\rho}_f \nabla_x \cdot u. \end{aligned}$$

Let us assume that *i)* holds. Since  $v$  is divergence free, we obtain

$$\partial_t \phi + \nabla_x \cdot (\phi u) = \frac{\bar{\rho}_f}{\bar{\rho}_d - \bar{\rho}_f} \nabla_x \cdot (\kappa \nabla_x \ln(\bar{\rho}_f + (\bar{\rho}_d - \bar{\rho}_f)\phi)) = \frac{\bar{\rho}_f}{\bar{\rho}_d - \bar{\rho}_f} \nabla_x \cdot (\kappa \nabla_x \ln(\rho)).$$

Hence *ii)* holds with  $\tilde{\kappa} = \kappa \frac{\bar{\rho}_f}{\bar{\rho}_d - \bar{\rho}_f}$ . Conversely, assuming *ii)*, the mass conservation imposes

$$\nabla_x \cdot u = -\frac{\bar{\rho}_d - \bar{\rho}_f}{\bar{\rho}_f} \nabla_x \cdot (\tilde{\kappa} \nabla_x \ln(\bar{\rho}_f + (\bar{\rho}_d - \bar{\rho}_f)\phi)) = -\frac{\bar{\rho}_d - \bar{\rho}_f}{\bar{\rho}_f} \nabla_x \cdot (\tilde{\kappa} \nabla_x \ln(\rho)).$$

We conclude that *i)* holds.  $\square$

This statement is important because it implies that different choices of unknowns are equivalent which, in turn, can motivate different numerical strategies. Indeed, instead of working with density  $\rho$  and velocity  $u$  as numerical unknowns, it is equally relevant to solve the evolution PDEs for  $\phi$  and  $u$ , using  $\rho = \bar{\rho}_f + (\bar{\rho}_d - \bar{\rho}_f)\phi$ . Then the mass conservation (4) appears as the constraint that defines the pressure. We refer to [4, 24, 25] where this viewpoint is adopted. Beyond the description of mixture flows, the interested reader can find in Brenner’s papers [8, 9, 10, 11] the elements on a deep debate on the role of mean mass and mean volume velocity in fluid mechanics.

## 1.2 A hierarchy of models

Instead of working with (3), it can be convenient to consider instead a solenoidal velocity field. From now on, we set

$$v = u + \kappa \nabla_x \ln(\rho).$$

Then (1) becomes a convection–diffusion PDE

$$\partial_t \rho + \nabla_x \cdot (v \rho) = \kappa \Delta_x \rho. \tag{5}$$

For the momentum equation (2), we start by writing it in non conservative form

$$\rho(\partial_t u + (u \cdot \nabla_x)u) + \nabla_x p = \rho g + \text{Div}_x(\mu \mathbb{D}(u)).$$

Next, we observe that

$$\begin{aligned} \rho \partial_t u &= \rho \partial_t v - \kappa \rho \partial_t \nabla_x \ln(\rho) \\ &= \rho \partial_t v + \kappa \left( \nabla_x (v \cdot \nabla_x \rho) - \frac{\nabla_x \rho}{\rho} v \cdot \nabla_x \rho \right) - \kappa^2 \left( \nabla_x \Delta_x \rho - \frac{\nabla_x \rho}{\rho} \Delta_x \rho \right), \end{aligned}$$

while

$$\text{Div}_x(\mu \mathbb{D}(u)) = \text{Div}_x(\mu \mathbb{D}(v)) - \kappa \text{Div}_x(\mu D_x^2 \ln(\rho))$$

where, for a scalar function  $h : (t, x) \in (0, T) \times \mathbb{R}^N \mapsto h(t, x) \in \mathbb{R}$ , we denote by  $D_x^2 h$  the hessian matrix with components  $\partial_{x_i} \partial_{x_j} h(t, x)$ , and

$$\rho(u \cdot \nabla_x)u = \rho(v \cdot \nabla_x)v - \kappa \left( (\nabla_x \rho \cdot \nabla_x)v + \rho(v \cdot \nabla_x) \frac{\nabla_x \rho}{\rho} \right) + \kappa^2 (\nabla_x \rho \cdot \nabla_x) \frac{\nabla_x \rho}{\rho}.$$

Furthermore, we remark that

$$\nabla_x (v \cdot \nabla_x \rho) - \frac{\nabla_x \rho}{\rho} v \cdot \nabla_x \rho - \rho(v \cdot \nabla_x) \frac{\nabla_x \rho}{\rho} = \nabla_x v^T \nabla_x \rho.$$

Therefore we arrive at

$$\begin{aligned} \rho(\partial_t v + (v \cdot \nabla_x)v) + \nabla_x p &= \rho g + \text{Div}_x(\mu \mathbb{D}(v)) \\ &\quad + \kappa (\nabla_x v - \nabla_x v^T) \nabla_x \rho \\ &\quad + \kappa^2 \left( \nabla_x \Delta_x \rho - \text{Div}_x \left( \frac{\nabla_x \rho \otimes \nabla_x \rho}{\rho} \right) \right) \\ &\quad - \kappa \text{Div}_x(\mu D_x^2 \ln(\rho)). \end{aligned} \tag{6}$$

The system (5)–(6) completed by the condition  $\nabla_x \cdot v = 0$  is equivalent to (1)–(3). The advantage relies on the fact that we are dealing with a solenoidal velocity, but we have simplified the constraint at the price of introducing high order terms in the mass and momentum balance laws. For physical arguments favoring this formulation, we refer to [8, 9, 11].

Let us now detail various manipulations and simplifications that can be performed on the model.

- a) When the viscosity  $\mu$  is constant, the last term in (6) is a gradient:  $\kappa \text{Div}_x(\mu D_x^2 \ln(\rho)) = \kappa \mu \nabla_x \Delta_x \ln(\rho)$  which can be incorporated in the pressure, like the term  $\kappa^2 \nabla_x \Delta_x \rho$ . This is the situation treated in [30].

- b) A more relevant case consists in assuming that  $\mu$  is an affine function of  $\rho$ . It arises in particular when using the formula proposed in [23] for the effective viscosity of suspensions. According to [23], we have

$$\mu = \mu_\star \left(1 + \frac{N+2}{2} \phi\right) = \mu_\star \left(1 - \frac{N+2}{2} \frac{\bar{\rho}_f}{\bar{\rho}_d - \bar{\rho}_f} + \frac{N+2}{2(\bar{\rho}_d - \bar{\rho}_f)} \rho\right) = \bar{\mu} + \tilde{\mu} \rho \quad (7)$$

with  $\mu_\star$  the standard viscosity of the fluid, and  $N$  the space dimension. Like in a), the contribution in the last term of (6) associated to  $\bar{\mu}$  can be incorporated in the pressure. The perturbation reads

$$\tilde{\mu} \text{Div}_x(\rho D^2 \ln(\rho)) = \tilde{\mu} \left( \nabla_x \Delta_x \rho - \text{Div}_x \left( \frac{\nabla_x \rho \otimes \nabla_x \rho}{\rho} \right) \right).$$

The first term in the right hand side can disappear in the pressure gradient. With this assumption on  $\mu$ , which appears in [21], (6) can be recast as

$$\begin{aligned} \rho(\partial_t v + (v \cdot \nabla_x)v) + \nabla_x p &= \rho g + \text{Div}_x(\mu \mathbb{D}(v)) \\ &\quad + \kappa(\nabla_x v - \nabla_x v^T) \nabla_x \rho \\ &\quad + \kappa(\kappa - \tilde{\mu}) \text{Div}_x \left( \frac{\nabla_x \rho \otimes \nabla_x \rho}{\rho} \right). \end{aligned} \quad (8)$$

- c) The Kazhikov-Smagulov model [38] is obtained by neglecting the last term in the right hand side of (8), which contains the higher nonlinearities and derivatives with respect to  $\rho$ . This can be motivated by assuming  $0 < \kappa \ll 1$  and  $0 < \tilde{\mu} \ll 1$  (or  $\tilde{\mu} = 0$  as in [30, 38]). The later makes sense with Einstein's formula (7) in the regime  $\bar{\rho}_d/\bar{\rho}_f \gg 1$ . The Kazhikov-Smagulov system is analyzed in [5, Chap. 3, Sect. 4, sp. Theorem 4.1] for the case where  $\mu$  is constant: assuming  $\kappa < 2 \frac{\mu}{\rho_+ - \rho_-}$ , where  $0 < \rho_\pm < \infty$  stand for the extreme values of the initial density, the global existence (and uniqueness in dimension 2) of a weak solution is established. The local existence of smooth solutions is investigated in [6, 50, 51]. Ref. [21] gets rid of the last term in (8) by postulating a ad hoc relation between the coefficient  $\kappa$  and  $\tilde{\mu}$ , namely assuming  $\kappa = \tilde{\mu}$ . Not only this assumption simplifies the model, but it also leads to a remarkable balance law for the energy of the system, see [21, Section 2.2]. The mathematical analysis of this specific case is due to [12].
- d) A further simplification arises by pushing forward the asymptotic regime in c). We get rid of all  $\mathcal{O}(\kappa)$  terms, but in the mass conservation. We obtain this way the Graffi model [34]

$$\begin{aligned} \partial_t \rho + \nabla_x \cdot (\rho v) &= \kappa \Delta_x \rho, \\ \rho(\partial_t + (v \cdot \nabla_x)v) + \nabla_x p &= \rho g + \bar{\mu} \text{Div}_x(\mathbb{D}(v)), \\ \nabla_x \cdot v &= 0. \end{aligned} \quad (9)$$

A derivation of (9) from (5) and (8), with the divergence free constraint, is proposed in [30] in the regime of small Graffi number  $\mathcal{G} = \frac{\bar{\mu} \kappa}{g \bar{\rho}_f L^3} \ll 1$ , with  $L$  a certain length of reference.



Kazhikov-Smagulov equations have been introduced in order to model pollution spread in atmospheric flows or contaminant spread in groundwater, with further analysis on the instability of certain layered configuration [30]. The model (10) has also been proposed to simulate the formation of powder-snow avalanches [21]. It also appeared in a slightly different form in [24, 25]. It is noteworthy that (10) does not rely on any Boussinesq-type hypothesis that would restrict the applicability to flows with small density ratio. For real avalanches, the Reynolds number  $\text{Re}$  can be as large as  $10^8$  and the densimetric Froude number  $\text{Fr}_d$  is close to 1. However, for experimental devices in laboratory, the values of the parameters are less extreme with  $\text{Re} \approx 10^4$  and  $\text{Fr}_d \approx 1$  ( $\Delta\rho/\rho_- \approx 0.2$ ), see [43, 45]. These laboratory values are affordable for numerical experiments. Clearly, there are uncertainties in the evaluation of the Schmidt number, because it highly relies on modeling assumptions. In all what follows, we shall set

$$\text{Sc} = 1$$

(in [43],  $\text{Sc} = 0.7$  is adopted for the simulation of avalanches). The goal of this section is to describe the numerical scheme used to solve such a system, and to validate both the model and the scheme by comparing our numerical results to analytical or experimental ones.

The equations are set on a bounded domain  $\Omega_\star \subset \mathbb{R}^N$  ( $N = 2$  in the numerical experiments below). The definition of relevant boundary conditions that complete (10) is definitely a delicate modeling question. All the simulations discussed below are performed by using the no-slip boundary condition for the velocity field and the Neumann boundary condition for the density

$$v_\star|_{\partial\Omega_\star} = 0, \quad \nabla_{x_\star}\rho_\star \cdot \vec{n}|_{\partial\Omega_\star} = 0 \tag{11}$$

with  $\vec{n}$  the outward normal unit vector on  $\partial\Omega_\star$ . As a matter of fact, (11) ensures that there is no mass influx, and the total mass is conserved by the system:  $\frac{d}{dt_\star} \int_{\Omega_\star} \rho_\star(t_\star, x_\star) dx_\star = 0$ . These boundary conditions are equally used for the mathematical investigation of the problem in [5, 12, 35]. They also complete the system (10) for the simulations of avalanches in [21]. In [24, 25], the Neumann boundary condition is maintained for the density, but the no-slip condition is imposed on the mean mass velocity  $u_\star = v_\star - \frac{1}{\text{ReSc}} \nabla_{x_\star} \ln(\rho_\star)$ . It also makes sense to impose a friction law, characterized by a coefficient  $0 < \alpha < 1$ , on the velocity

$$v_\star \cdot \vec{n}|_{\partial\Omega_\star} = 0, \quad [(1 - \alpha)v_\star + \alpha\mathbb{D}_\star(v_\star)\vec{n}] \cdot \vec{t}|_{\partial\Omega_\star} = 0,$$

with  $\vec{t}$  the tangential vector at  $\partial\Omega_\star$ , see [21], or its equivalent form on  $u_\star$ , see [24, 25]. To decide whether the mean mass or the mean volume velocity enters into the no-slip boundary condition is definitely a delicate modeling issue. In [9] it is argued that the boundary condition should be

$$u_\star \cdot \vec{n}|_{\partial\Omega_\star} = 0, \quad (\mathbb{I} - \vec{n} \otimes \vec{n})v_\star|_{\partial\Omega_\star} = 0.$$

## 2.1 Description of the scheme

Several numerical approaches are available for the numerical approximation of the solutions of (10). The simulations in [21] are realized with the open-source code `OpenFoam`; as far as we know the simulations are based on second order upwind finite volume scheme, performed on a fixed Cartesian grid (but we are not aware of the technical details of the whole scheme). Simulations of [45] are done with the commercial code `Fluent`, based on a Finite Element discretization with Cartesian grids. A dedicated code has been developed in [24, 25]. It uses Finite Element discretizations, coupled to a characteristic method to treat the convection terms. The scheme is coupled to mesh refinement procedures, in order to follow the displacement of the avalanche front. Reference [35] is concerned with numerical analysis purposes only; the proposed Finite Element scheme is not implemented. Here, we propose a mixed finite volume/finite element strategy. Such an hybrid scheme has been introduced in [14] for the resolution of the standard incompressible Navier-Stokes system with variable density<sup>1</sup>. Briefly, the algorithm is based on a time splitting, which allows us to discretize the density equation (10)-(i) by using a Finite Volume strategy and the momentum equation coupled with the constraint (10)-(ii)-(iii) by using a Finite Element approximation, with the classical choice of the Taylor-Hood finite element. This method has been improved in [13] with the design of multislope flux limiters for transport equations, so that the maximum principle still holds on the discrete system for fully unstructured meshes. This property is absolutely crucial to consider flows with high density contrasts and to follow fronts by a mesh refinement method. We also refer to [4] where a quite similar approach has been developed, with a different finite volume approximation of the convection terms. We wish to adapt the scheme described in [13, 14] in order to explore numerically the system (10).

**Remark 1** *Besides the design of the numerical method, the choice of the independent unknowns and the discrete formulation of the problem is certainly far from harmless. Here, we decide to work with the density  $\rho$  and the solenoidal velocity  $v$ , like in [21]. This is by contrast with [4, 24, 25] which use instead the diffusion equation satisfied by the volume fraction  $\phi$ , and the mean mass velocity  $u$ , see Lemma 1, the mass conservation equation satisfied by  $\rho$  being seen as a constraint.*

From now on, we restrict the discussion to the two-dimensional framework. We consider a mesh of the computational domain made of triangles. We associate to this primal mesh the dual mesh obtained by joining the barycenters of the triangles to the midpoints of the edges, see Figure 1. The elements of this tessellation are the control volumes of the finite volume approximation: the discrete density is intended to approximate the mean-value of the physical density over the control volumes. Note that the discrete densities are stored at the vertices of the primal mesh (Vertex-Based method).

As written above, the algorithm is based on a time splitting. At time  $t_x^n$ , we have at hand a discrete evaluation of the density  $\rho_h^n$  and of the velocity-pressure field  $(v_h^n, p_h^n)$ . We start by updating

---

<sup>1</sup>An Open-Source version of the code dealing with 2D Incompressible Navier-Stokes equations with variable density is available at the URL: <http://math.univ-lille1.fr/~simpaf/SITE-NS2DDV/home.html>

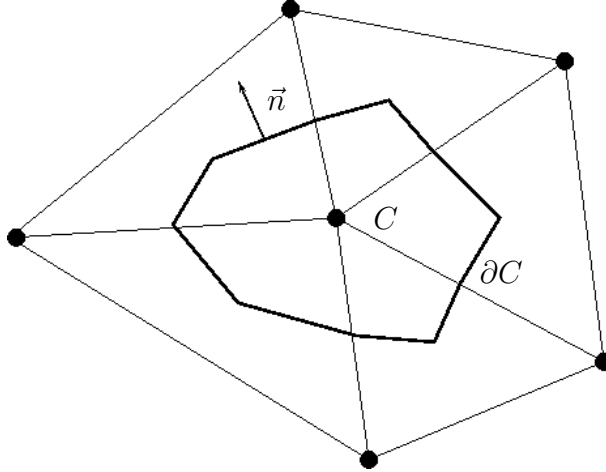


Figure 1: The finite volume control volume.

the density, thus defining  $\rho_h^{n+1}$  by using (10)-(i). We remind that the density is piecewise constant on the control volumes. Compared to the case of pure transport, we have to compute in addition the diffusive fluxes through the interfaces of the control volumes. In other words, given a volume control  $C$ , we need to define a discrete version of the flux

$$\frac{1}{\text{ReSc}} \int_{\partial C} \nabla_{x^*} \rho_{x^*} \cdot \vec{n} \, d\sigma, \quad (12)$$

where  $\vec{n}$  stands for the outward normal unit vector on  $\partial C$ . To this end, we interpret the density as a piecewise  $\mathbb{P}_1$  function on each triangle of the primal mesh. It allows to properly define the value of (12) on each component of  $\partial C$ . This idea is reminiscent of the so-called FVE method for the discretization of convection-diffusion equations [18, 26, 28], and [27, Section 3.4.3]. The convection term is treated according to the method described in [13, 14]. The construction of the transport scheme relies on the MUSCL framework, but it involves a quite elaborate definition of limiters so that the maximum principle is satisfied on 2D unstructured meshes, under a suitable convective CFL condition, according to the analysis in [13]. Diffusion is treated implicitly so that we can expect it does not deteriorate the stability condition. Note that the preservation of the discrete maximum principle by such finite volume methods for convection-diffusion equation is a delicate question. It might induce some restrictions on the meshes, or require a more refined definition, possibly non-linear, of the diffusion fluxes. The use of such elaborate schemes is beyond the scope of this work; a detailed exposition of the state of the art can be found in [20] and the references therein. The time discretization is based on the Adam-Bashforth scheme for the transport term and the Crank-Nicolson scheme for the diffusive term, which formally leads to second-order consistency.

Once  $\rho_h^{n+1}$  is computed, the second step of the splitting updates the velocity field and the pressure by using a Finite Element approximation of (10)-(ii)-(iii). The time discretization is based on the BDF second order scheme. Compared to the classical variable density incompressible Navier-Stokes system, see [14, 13], we have to compute in addition the term corresponding to

$$\frac{1}{\text{ReSc}}(\nabla_{x_\star} v_\star - \nabla_{x_\star} v_\star^T) \nabla_{x_\star} \rho_\star \quad (13)$$

arising in the right-hand-side of (10)-(ii). Again, we use the interpretation of the density as a continuous and piecewise- $\mathbb{P}_1$  function on the primal mesh. Then, a classical assembly procedure defines the finite element formulation of (13). In practice, a more sophisticated time-splitting can be used in order to preserve the global second-order accuracy both in time and space (the so-called Strang splitting, see [14]).

## 2.2 Validation of the Scheme: Comparison to an Exact Solution

First of all, we evaluate the ability of the scheme to recover an analytical solution and we check the corresponding rates of convergence when dealing with smooth solutions. The computational domain is the square  $\Omega_\star = [-1, 1]^2$ . The explicit solution we wish to capture is given by

$$\begin{cases} \rho_{\text{ex}}(x_\star, y_\star, t_\star) &= 2 + \cos x_\star \sin y_\star \sin t_\star, \\ v_{\text{ex}}(x_\star, y_\star, t_\star) &= (-4y_\star(x_\star^2 - 1)^2(y_\star^2 - 1), 4x_\star(y_\star^2 - 1)^2(x_\star^2 - 1))^T, \\ p_{\text{ex}}(x_\star, y_\star, t_\star) &= \sin x_\star \sin y_\star \sin t_\star. \end{cases} \quad (14)$$

We solve the set of equations (10) on the time interval  $0 \leq t_\star \leq 0.2$ . The dimensionless parameters are all set to unity:  $\text{Re} = \text{Fr} = \text{Sc} = 1$ . Like in [21], we suppose that the viscosity depends affinely on the density:  $\mu_\star(\rho_\star) = 1 + \rho_\star/2$ . The appropriate source terms  $f_\star^{(1)}$  and  $f_\star^{(2)}$  are added in the right-hand side of the two first equations in (10), so that (14) is indeed a solution. We work with unstructured meshes. The time step  $dt_\star$  is proportional to  $h_{\star, \min}$ , the length of the smallest edge in the mesh, so that the CFL stability criterion is always ensured.

Figure 2 displays the values of the maximal error recorded during the time interval given as a function of  $h_{\star, \max}$ , the length of the largest edge in the mesh. Errors are here evaluated with the  $L^2(\Omega_\star)$ -norm, namely  $\|\rho_{\text{ex}} - \rho_h\|_{L^2(\Omega_\star)}$ ,  $\|v_{\text{ex}} - v_h\|_{L^2(\Omega_\star)}$  and  $\|p_{\text{ex}} - p_h\|_{L^2(\Omega_\star)}$ . On this numerical experiment, the scheme is globally second-order accurate. More precisely, the convergence rates with respect to  $h_{\star, \max}$  between the two finest grids for the density, velocity and pressure are respectively equal to 2.04, 2.44 and 2.30. It agrees with a similar result obtained for the incompressible Navier-Stokes system with variable density, resolved with the same kind of numerical scheme (see [13]). Hence, the treatment of (12) and (13) does not alter the accuracy of the scheme.

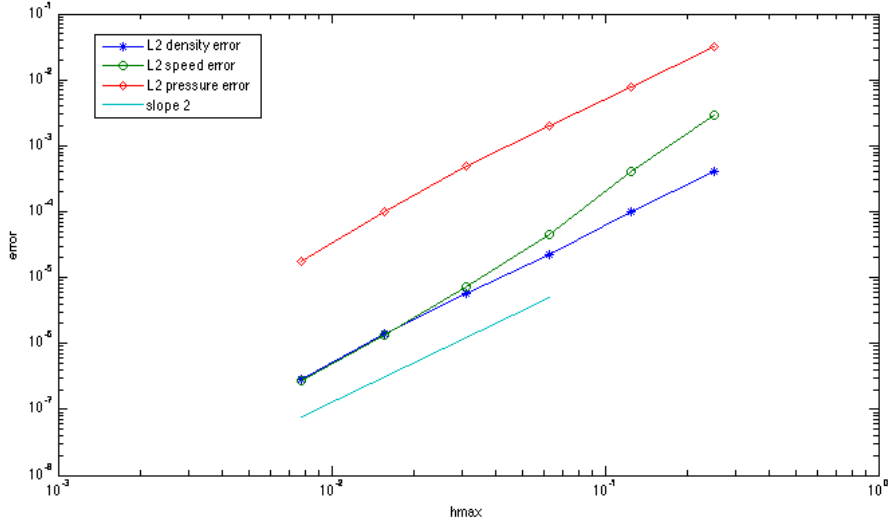


Figure 2: Convergence rates of the numerical scheme for the analytical solution.

## 2.3 Simulations of Avalanches: Parametric Study on the Froude and Reynolds Numbers

In this Section, we wish to discuss the role of the Froude and Reynolds numbers (we remind that the Schmidt number  $Sc$  is set to 1). To this end, we shall compare the simulations with experimental data available in [43, 45]. Further experimental data can be found e. g. in [16]. We make use of the system (10) where we assume a constant viscosity  $\mu_*(\rho_*) \equiv 1$ . The boundary conditions (Dirichlet for the velocity, Neumann for the density) are given by (11).

Let us describe the data, extracted from [43, 45], in physical units. The physical domain is the rectangle  $\Omega = [0, 2.0 m] \times [0, 0.5 m]$ . The fluid is initially at rest, and the initial condition on the density is given by:

$$\rho_0(x, y) = \begin{cases} \rho_+ & \text{for } 0 \leq x \leq 0.15 m \text{ and } 0 \leq y \leq 0.09 m, \\ \rho_- & \text{otherwise,} \end{cases}$$

with  $\rho_+ = 1.2 kg m^{-3}$  and  $\rho_- = 1 kg m^{-3}$ . It yields  $\Delta\rho/\rho_- = 0.2$ . In order to define the Reynolds and Froude coefficients we need length and time units. The length of reference is defined by the initial height of the avalanche:  $L = 0.09 m$ , and we define the characteristic velocity of the flow as the average measured velocity of the avalanche front (see [43, 45]):  $U = 0.35 m s^{-1}$ . We have  $\|g\| = 9.8 m s^{-2}$  and the slope of the ground is defined by  $g/\|g\| = (\sin 10^\circ, -\cos 10^\circ)^T$ . Due to scale factors, the laboratory avalanches do not reproduce the physical characteristics of real flows. Experiments reported in [43, 45] are performed using water flows with a complex kaolin-water

suspension representing the heavy fluid. The viscosity of such a mixture is not known. To start with we set  $\bar{\nu} = 3.15 \times 10^{-5} m^2 s^{-1}$ . This set of data leads to

$$\text{Fr}_d = 0.83, \quad \text{Fr} = 0.3725, \quad \text{Re} = 10^3.$$

It is likely that  $\text{Re} = 10^4$  would be more realistic for laboratory avalanches, to be compared to  $\text{Re} = 10^8$  for real avalanches, where the density ratio can be as large as 10. Of course, increasing the Reynolds number impacts the numerical cost. Note however that numerical comparison proposed in [43, 45] with a commercial code are based on a  $k/\epsilon$  model, where an enhanced effective viscosity is fitted to the experimental data, so that the definition we adopt here can be considered as quite fair, see also the comments below, when we make  $\text{Re}$  vary. Table 1 recaps the data and the dimensionless coefficients used for the simulation. In order to compare our results to the experimental data, we use three monitoring points  $A$ ,  $B$  and  $C$ , with location given in Table 1. From [43, 45] we have records at those points of the horizontal velocity. It will be compared to the corresponding numerical quantity, defined at the monitoring point  $A$  (and similarly for  $B$  and  $C$ ) by:

$$u_{\star A} = v_{\star A} - \frac{1}{\text{ReSc}} (\nabla_{x_{\star}} \ln(\rho_{\star}))_A.$$

The computational time step is set to  $dt_{\star} = 10^{-2}$ , and an adaptive mesh refinement strategy is used in order to follow the avalanche front. The computational effort (immediately sensible through the computational time) increases as the Reynolds number increases or the Froude number decreases. For the simulations presented here, the minimum length of the edges in the mesh oscillates around  $h_{\star, \min} \approx 0.002$  and the maximum one is of the order  $h_{\star, \max} \approx 0.17$ . The number of triangles in the mesh increases up to 40000 during the simulation. All convergence grid tests were previously performed to ensure that the mesh as well as the time step are fine enough to reach the grid convergence.

First of all, we set  $\text{Re} = 1000$  and we consider three Froude numbers, respectively  $\text{Fr} = 1.0$ ,  $0.6$  and  $0.3725$ . The isovalues of the density and the magnitude of the velocity field are displayed during the simulation, respectively in Figure 3 for  $\text{Fr} = 1.0$ , Figure 4 for  $\text{Fr} = 0.6$  and Figure 5 and 6 for  $\text{Fr} = 0.3725$ . These different Froude number values can be interpreted as the variation of the gravity vector magnitude, what leaves the Reynolds number unchanged. When the Froude number decreases, the strength of the external force increases and an acceleration of the avalanche front is observed, according to the physical intuition. This can be seen in the evolution of the speed magnitude in Figures 3, 4 and 5, and also in the amplitude of the horizontal velocity at the monitoring points in Figure 7 (on which the horizontal scale is not the same according to the Froude number involved). We point out that the results are displayed in the dimensional units, and the physical time needed to carry out each of these three simulations is clearly not the same. In particular, the avalanche hits the far right end boundary at  $t \approx 27$ s for  $\text{Fr} = 1.0$  and only at  $t \approx 10$ s for  $\text{Fr} = 0.3725$ . The numerical results obtained with  $\text{Fr} = 0.3725$  should be compared to the experimental data in [45, pages 53-54 and 58-59] (corresponding equivalently to  $\text{Fr}_d \approx 0.8329$ ).

Physical values	Dimensionless values
$L = 0.09 \text{ m}$	$L_\star = 1.00$
$U = 0.35 \text{ m s}^{-1}$	$U_\star = 1.00$
$T = L/U = 0.2571 \text{ s}$	$T_\star = 1.00$
$g = 9.81(\sin 10^\circ, -\cos 10^\circ)^T \text{ m s}^{-2}$	$g_\star = (\sin 10^\circ, -\cos 10^\circ)^T$
$\rho_+ = 1.2 \text{ kg m}^{-3}$	$\rho_{\star+} = 1.2$
$\rho_- = 1.0 \text{ kg m}^{-3}$	$\rho_{\star-} = 1.0$
$\Omega = [0, 2.0 \text{ m}] \times [0, 0.5 \text{ m}]$	$\Omega_\star = [0, 22] \times [0, 5.5]$
$(x_A, y_A) = (112 \text{ cm}, 2.7 \text{ cm})$	$(x_{\star A}, y_{\star A}) = (12.44, 0.30)$
$(x_B, y_B) = (112 \text{ cm}, 6.6 \text{ cm})$	$(x_{\star B}, y_{\star B}) = (12.44, 0.74)$
$(x_C, y_C) = (158 \text{ cm}, 2.7 \text{ cm})$	$(x_{\star C}, y_{\star C}) = (17.55, 0.30)$

Table 1: Physical values and dimensionless values.

In particular, we observe that the avalanche front moves forward at a very similar speed. Qualitatively, the mesh refinement strategy used in the simulation allows to capture the complex structures of the physical Kelvin-Helmholtz and Rayleigh-Taylor instabilities occurring in the vicinity of the front. Remark that the maximal speed is usually observed behind the front, and it can reach a noticeably larger value than the front speed, see [21, 24, 25, 36, 43] for similar observations. We also note on the velocity snapshots that a large domain is affected by the avalanche motion, a significant part of the surrounding light fluid is dragged by the snow release.

Second of all, we set  $Fr = 1.0$  and we make the Reynolds number vary. It corresponds to variation of the kinematic viscosity  $\bar{\nu}$ , all the other physical parameters remaining the same. The isovalues of the density and the magnitude of the velocity field are displayed during the simulation, respectively in Figure 3 for  $Re = 1000$ , Figure 8 for  $Re = 3000$  and Figure 9 for  $Re = 5000$ . Figure 10 shows the amplitude of the horizontal velocity at the monitoring points. In this picture, the horizontal and vertical scales are the same for the three simulations. As for the classical Navier-Stokes simulations, when the Reynolds number increases the velocity of the avalanche front remains qualitatively the same, but the motion presents more vortices and turbulent structures (which thus would need finer meshes to resolve the fine scales). This is confirmed in Figure 10: locally at the monitoring points the structure of the velocity field is more complicated when the Reynolds coefficient increases.

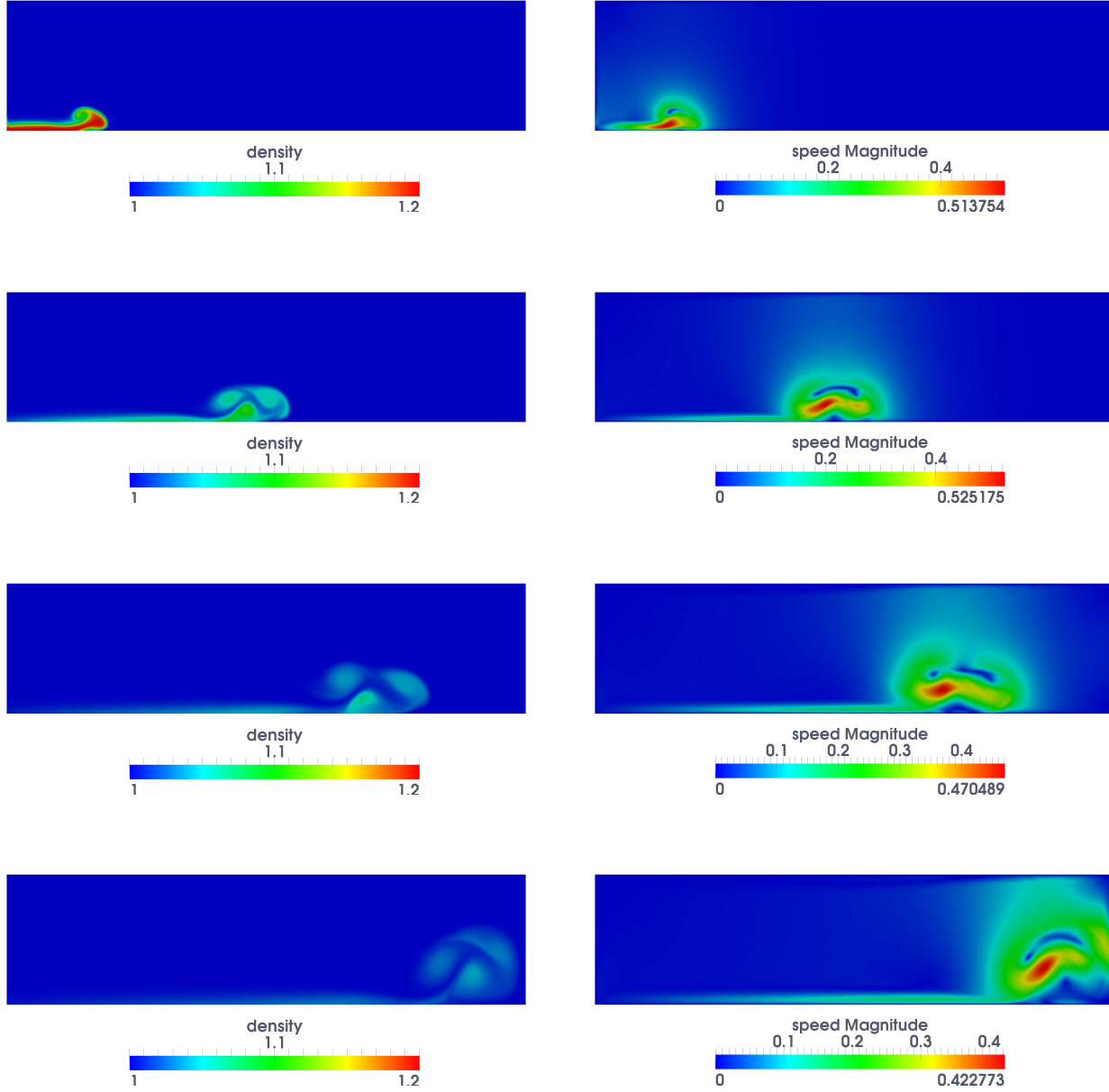


Figure 3: Density (left column) and speed magnitude (right column) at times  $t=2.8$  s,  $10.7$  s,  $19$  s and  $26.9$  s (from top to bottom) with  $Fr = 1.0$  and  $Re = 1000$ .

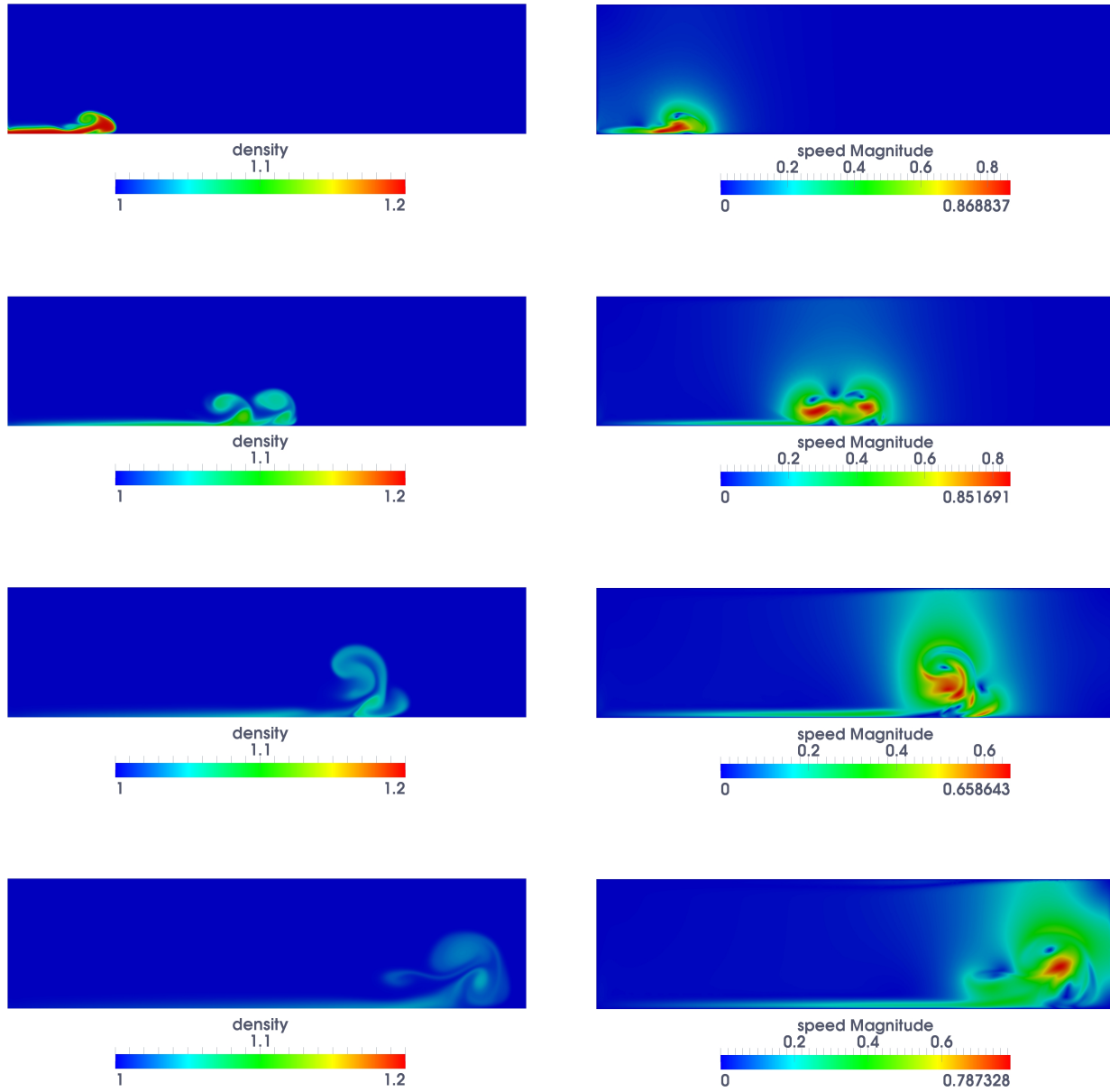


Figure 4: Density (left column) and speed magnitude (right column) at times  $t=1.79$  s, 6.42 s, 11.31 s and 16.19 s (from top to bottom) with  $Fr = 0.6$  and  $Re = 1000$ .

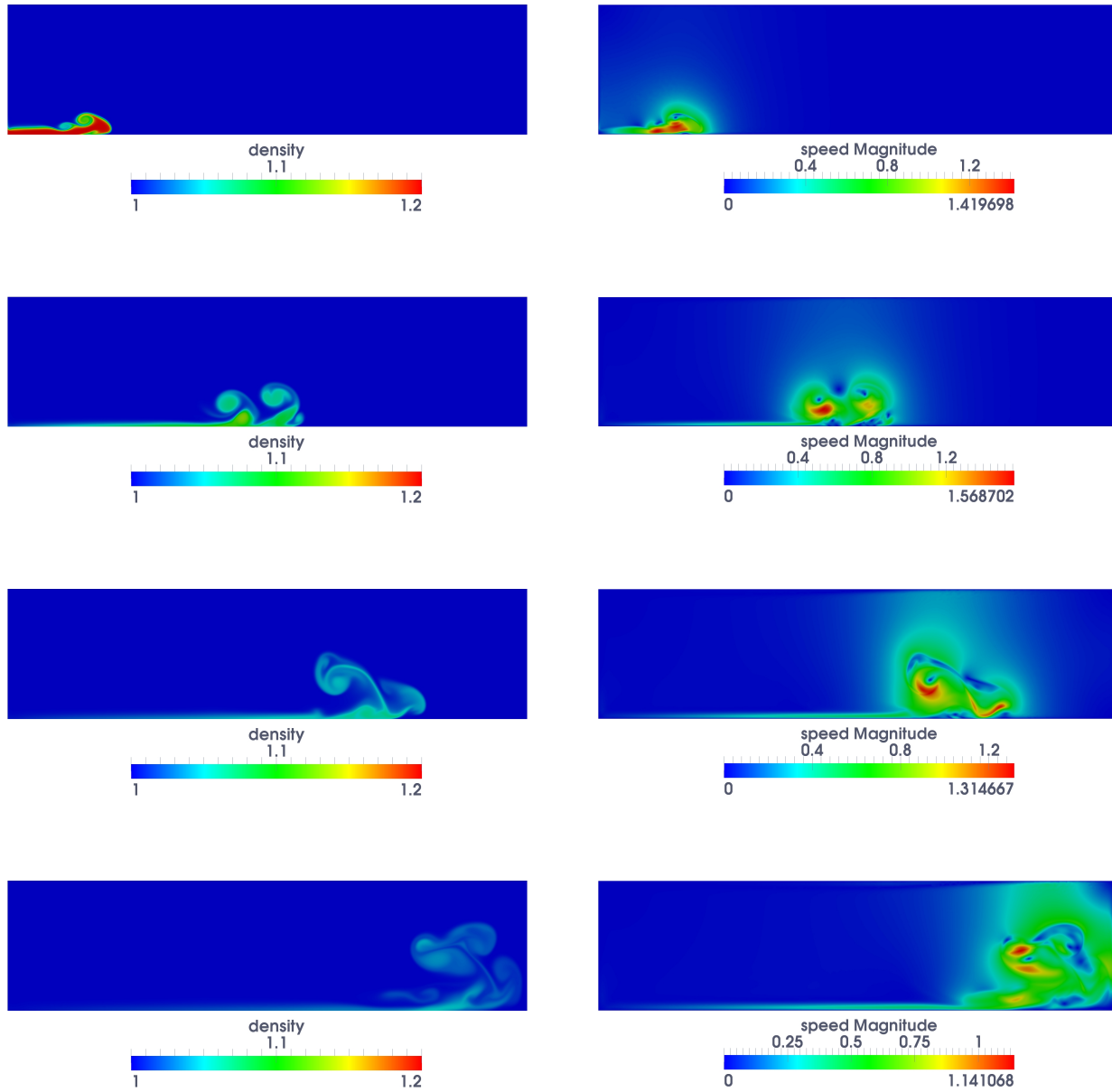


Figure 5: Density (left column) and speed magnitude (right column) at times  $t=1$  s, 4 s, 7 s and 10 s (from top to bottom) with  $Fr = 0.3725$  and  $Re = 1000$ .

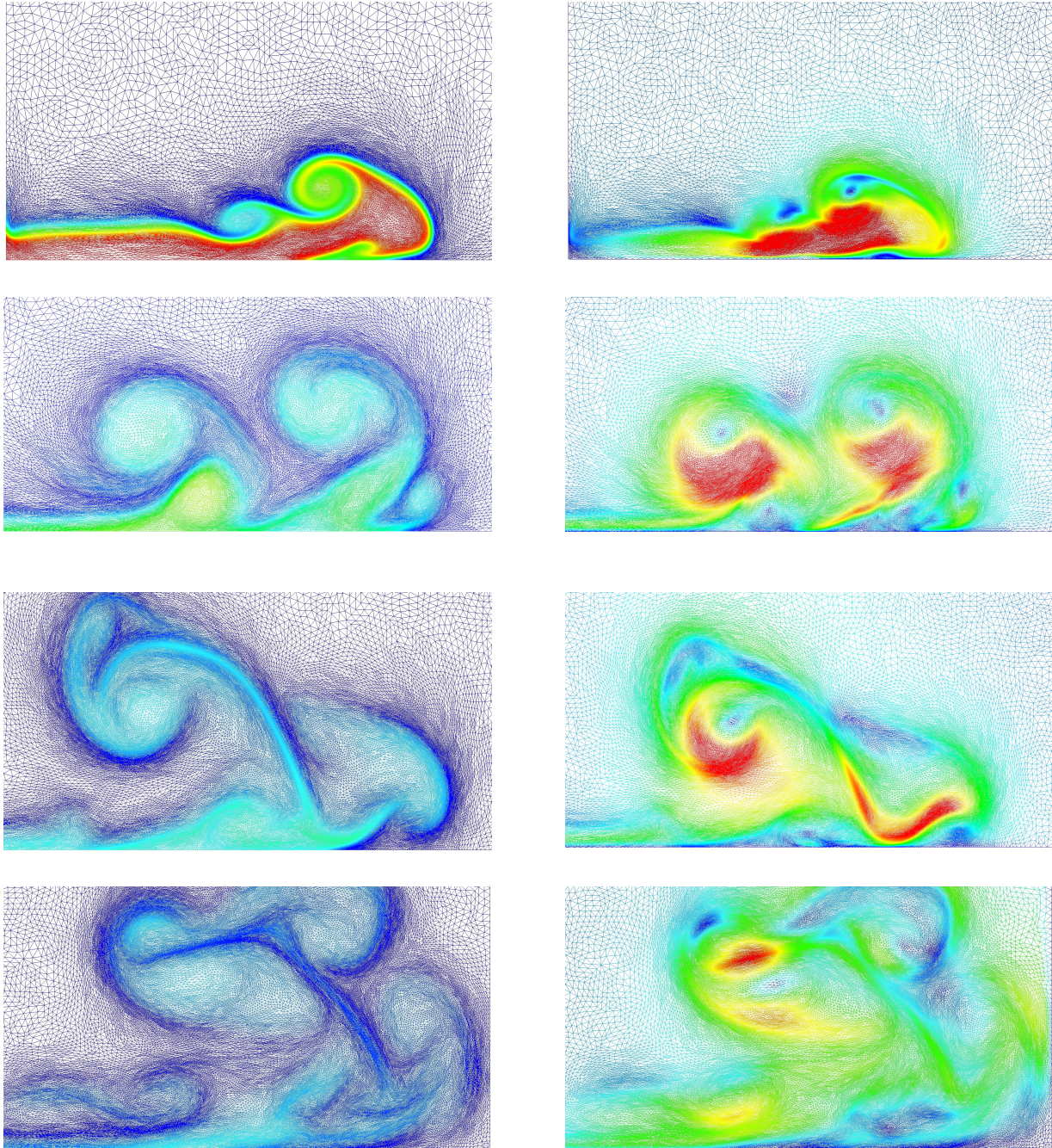


Figure 6: Local zooms in domain  $\Omega_*$  showing the meshes used for the calculation of density (left column) and speed magnitude (right column) at times  $t=1$  s, 4 s, 7 s and 10 s (from top to bottom) with  $Fr = 0.3725$  and  $Re = 1000$ . The color legends correspond to those used in Figure 5.

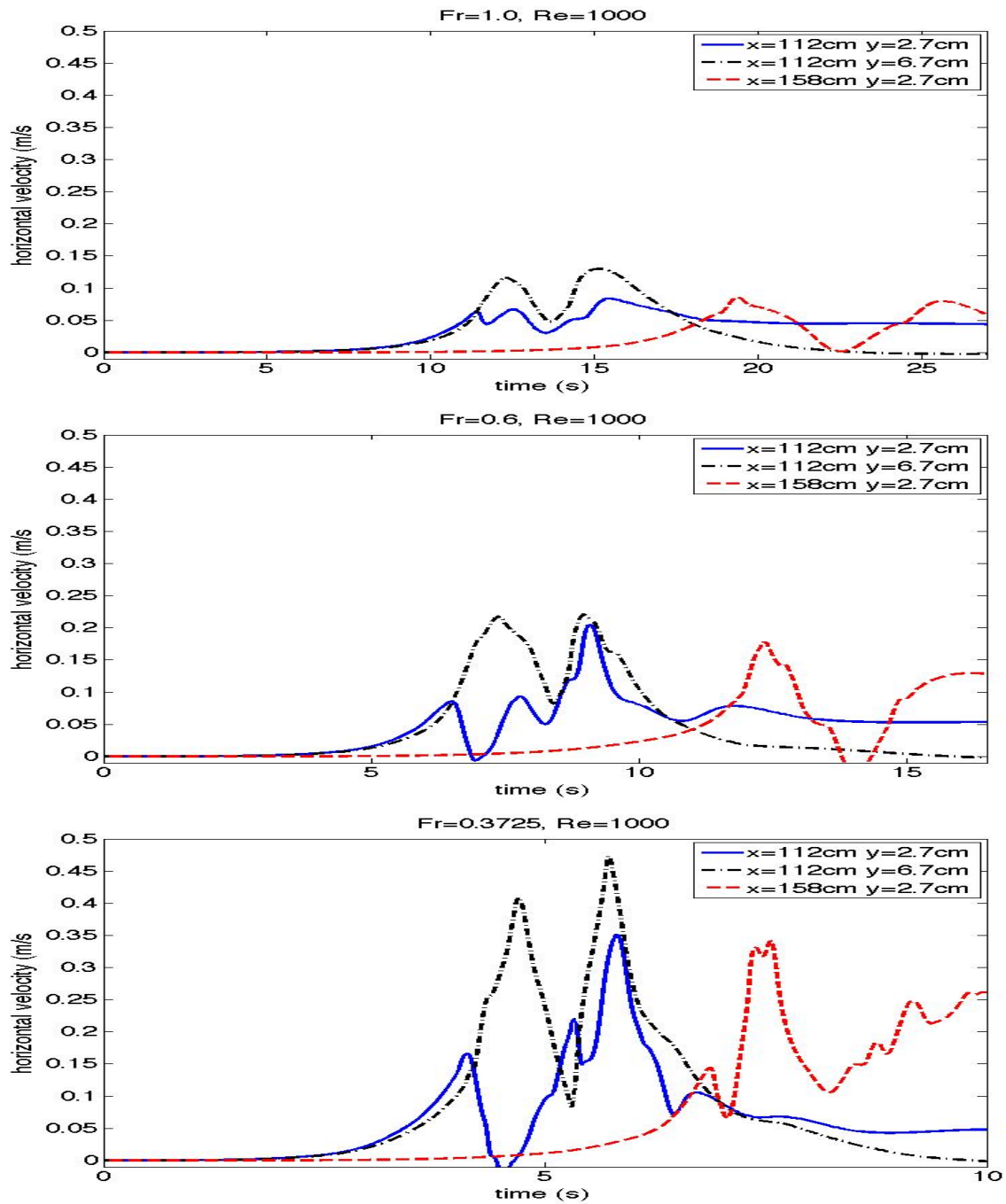


Figure 7: Evolution in time (seconds) of the physical horizontal velocity at the monitoring points  $A$  (blue),  $B$  (green),  $C$  (red), using  $Fr$  respectively equal to 1.0, 0.6 and 0.3725, from top to bottom.

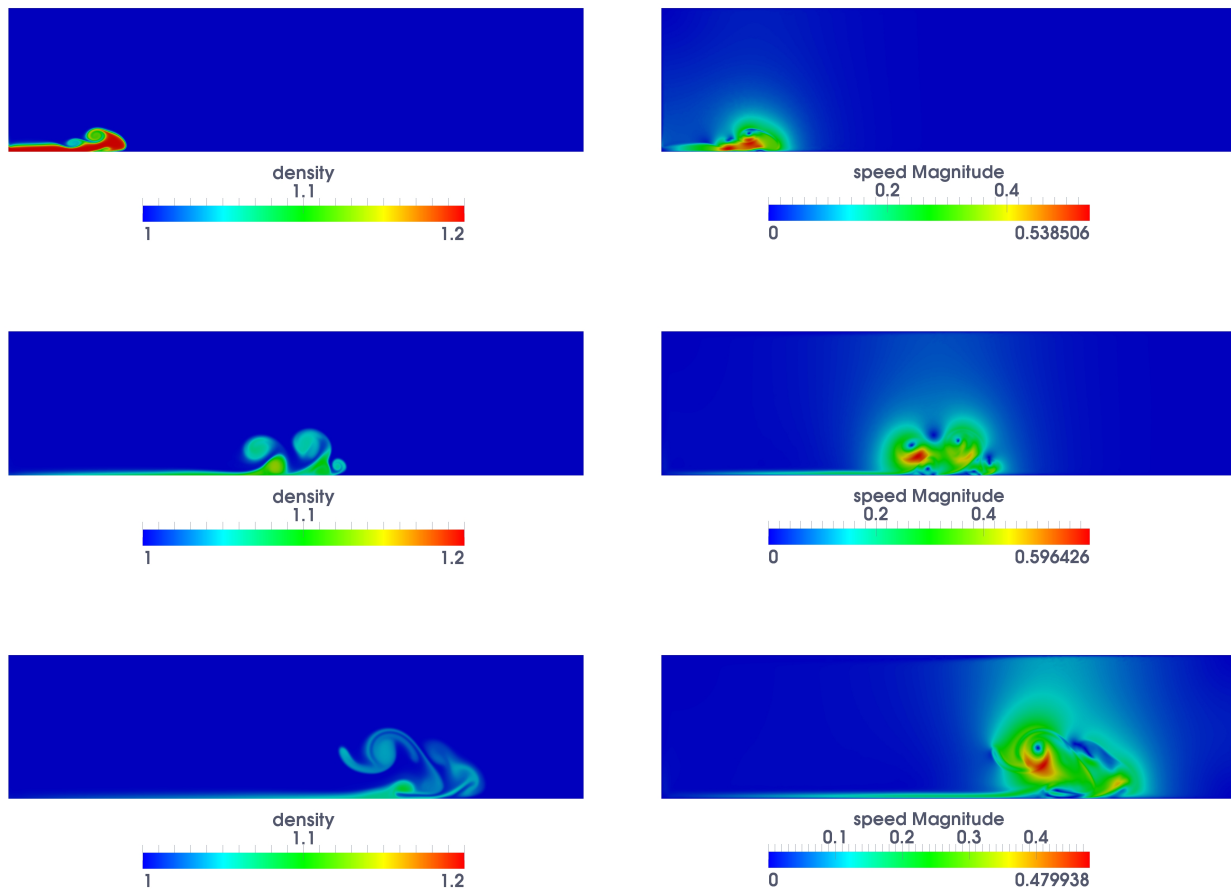


Figure 8: Density (left column) and speed magnitude (right column) at times  $t=2.8$  s, 10.7 s and 19 s (from top to bottom) with  $Fr = 1.0$  and  $Re = 3000$ .

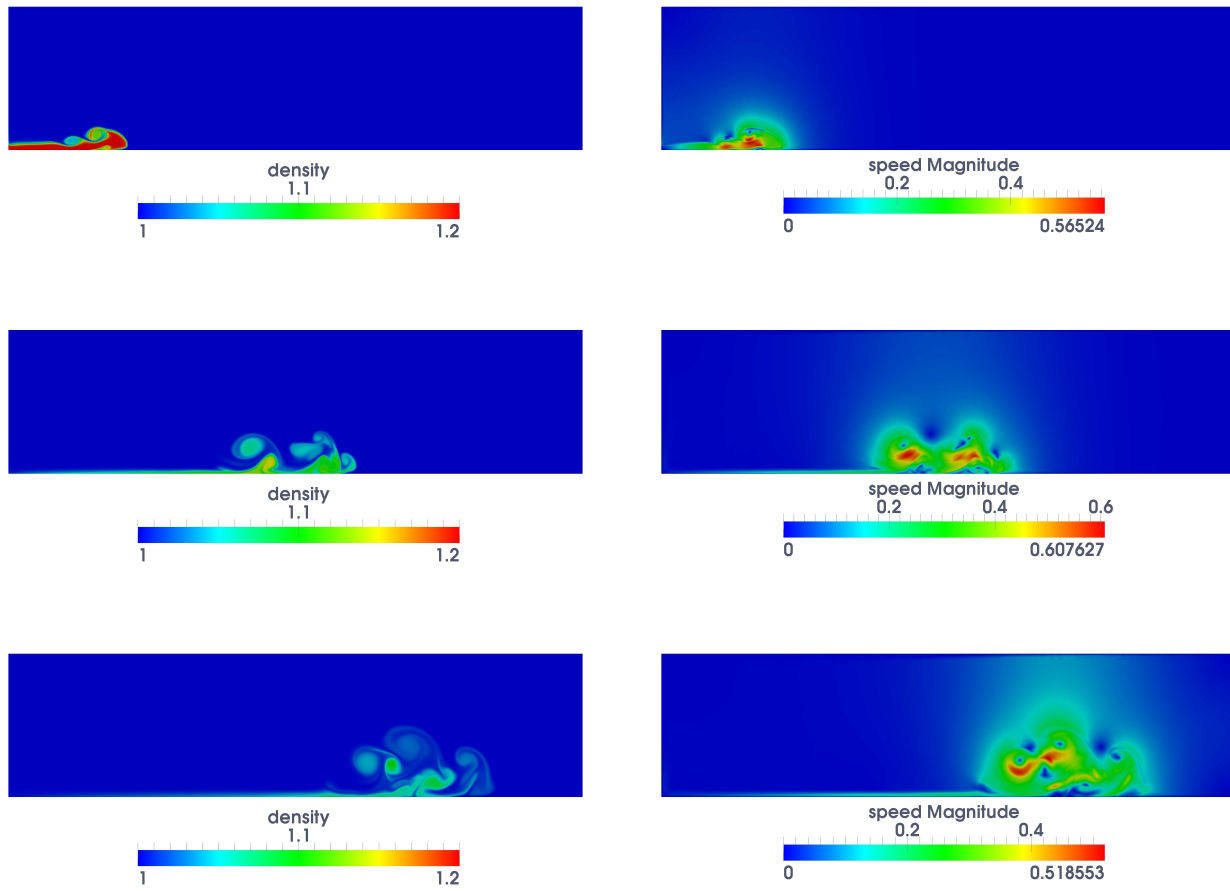


Figure 9: Density (left column) and speed magnitude (right column) at times  $t=2.8$  s, 10.7 s and 19 s (from top to bottom) with  $Fr = 1.0$  and  $Re = 5000$ .

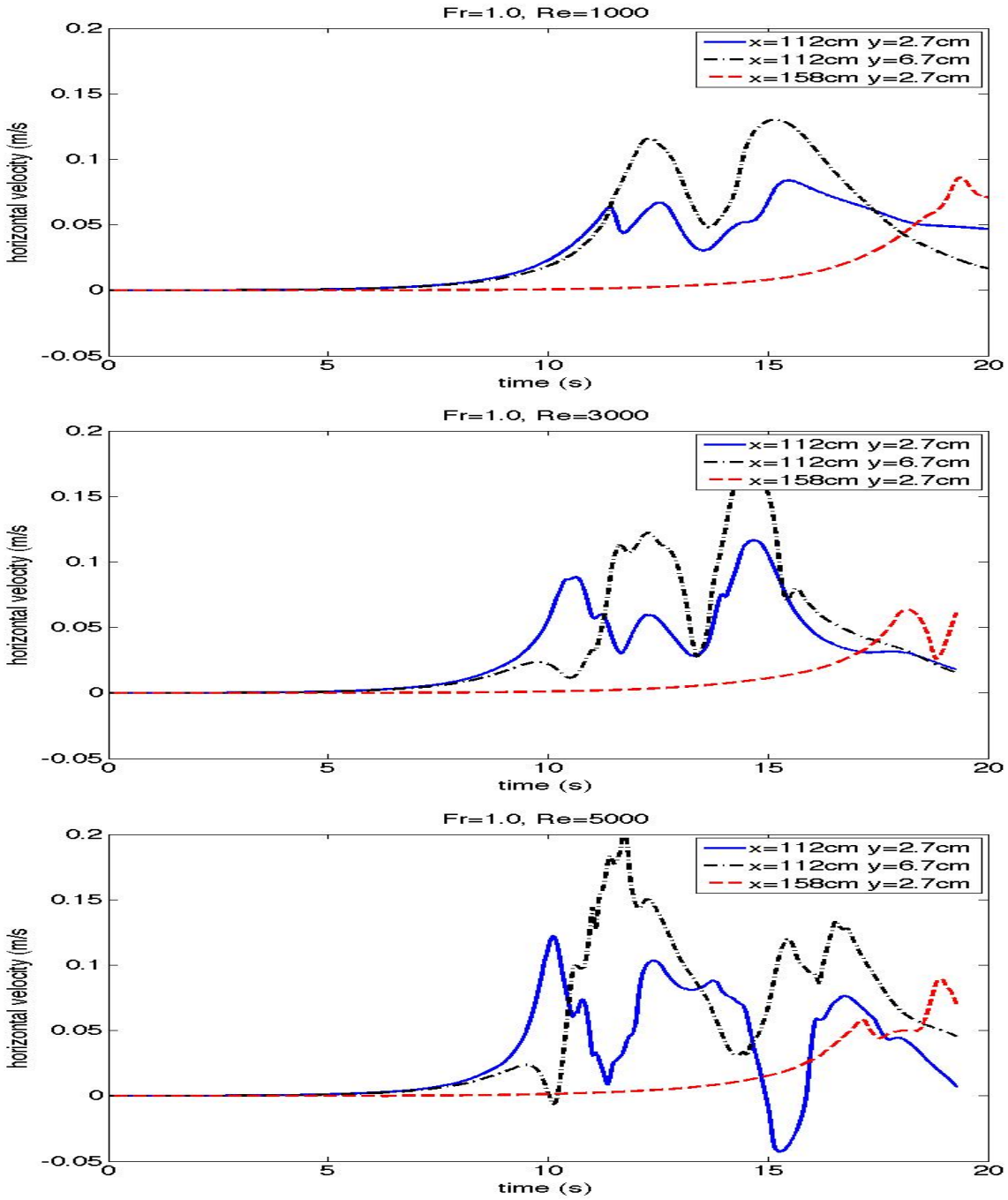


Figure 10: Evolution in time (seconds) of the physical horizontal velocity at the monitoring points  $A$  (blue),  $B$  (green),  $C$  (red), using  $Re$  respectively equal to 1000, 3000 and 5000, from top to bottom.

## 2.4 Simulation of Avalanches: Interaction with an Obstacle

We turn to the simulation of the interaction of an avalanche with an obstacle, a benchmark presented in [21]. In order to have a direct comparison we go back to the physical quantities. Namely, we consider the system

$$\begin{cases} \partial_t \rho + \nabla_x \cdot (v\rho) &= \nabla_x \cdot (\kappa \nabla_x \rho), \\ \rho(\partial_t v + (v \cdot \nabla_x)v) + \nabla_x p &= \rho g + \text{Div}_x(\mu \mathbb{D}(v)) + \kappa(\nabla_x v - \nabla_x v^T) \nabla_x \rho, \\ \nabla_x \cdot v &= 0, \end{cases}$$

completed by (11): homogeneous Dirichlet boundary condition on the velocity field, and homogeneous Neumann boundary condition on the density field.

The physical framework is quite similar to the one dealt with in Section 2.3: a heavy fluid flows under the effect of the gravity force along an inclined channel, but here the flow interacts with an obstacle. This kind of simulation is motivated by the dimensioning of protection devices. We refer to the schematic representation in Figure 11. The parameters are specified in Table 2. In particular, it should be noted that initially, the heavy fluid ( $\rho = \rho_+$ ), located in the rectangle  $[2l_0/3, h_0/3]$  is surrounded by a fluid with intermediate density  $\tilde{\rho} = \rho_- + 0.4(\rho_+ - \rho_-)$ . This configuration is intended to roughly mimic the observed layers in actual avalanches, with dense snow on the ground, topped by a fluidized bed that might degenerate to an aerosol flow.

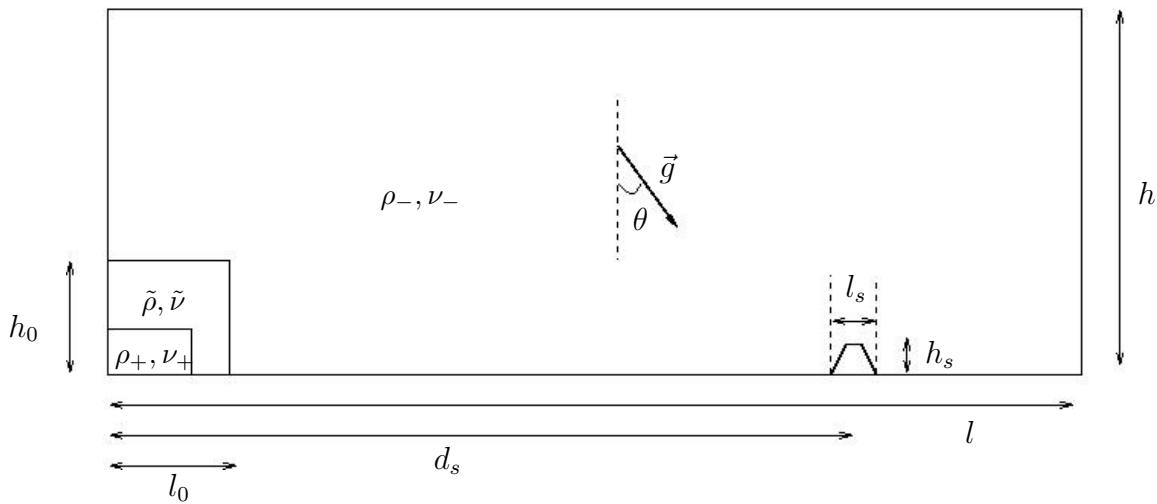


Figure 11: Domain and initial data configurations.

We take :

$$\kappa = 2\bar{\nu} \quad \text{with} \quad \bar{\nu} = \frac{\nu_+ \rho_+ - \nu_- \rho_-}{\rho_+ - \rho_-}, \quad \text{and} \quad \mu = 2\bar{\nu} \rho.$$

Gravity acceleration $\ g\ , m s^{-2}$	9.8
Slope of the inclined channel $\theta, ^\circ$	32
Heavy fluid density $\rho_+, kg m^{-3}$	20
Light fluid density $\rho_-, kg m^{-3}$	1
Heavy fluid kinematic viscosity $\nu_+, m^2 s^{-1}$	$4, 8 \cdot 10^{-4}$
Light fluid kinematic viscosity $\nu_-, m^2 s^{-1}$	$1, 0 \cdot 10^{-4}$
Domain height $h, m$	0.8
Domain length $l, m$	2.7
Initial avalanche height $h_0, m$	0.3
Initial avalanche length $l_0, m$	0.3
Obstacle height $h_s, m$	0.06
Obstacle thickness $l_s, m$	0.04
Obstacle distance $d_s, m$	1.92

Table 2: Avalanche simulation : physical parameters.

Concerning the numerical parameters, the mesh is made of an unstructured tessellation of triangles, and the smallest edge is about  $h_{\min} \approx 7 \times 10^{-4} m$ . The mesh evolves dynamically in order to follow the displacement of the front of the avalanche, with finer structures in the regions of large density gradients. The number of triangles in the mesh increases up to 15000 at the end of the simulation. The computational time step is set to  $dt = 10^{-3} s$ . We have performed a series of simulation by making both the time step and the mesh size vary in order to guaranty that the convergence grid is reached. Results are reported in Figure 12 where the isovalues of the density and the magnitude of the velocity are displayed.

We can observe a qualitatively satisfactory correspondence between the snapshots presented in Figure 12 and Figures 5 to 7 of [21], corresponding to the same physical data (the time scale has been erroneously reported in Fig- 5–7 of [21]; it needs to be corrected to fit with the data). The very first times of the simulation, we recognize the emergence of a classical elliptic front. Then during the sliding regime we can already observe the formation of Kelvin-Helmholtz instabilities, with a large vortex that takes place behind the head of the flow, above a zone of light density where the fluid is dragged by the avalanche. Finally, the interaction with the obstacle generates a jet directed upward, with the formation of the mushroom shape corresponding to a classical Rayleigh-Taylor instability. As it has been already pointed elsewhere, both from numerical or experimental studies [21, 24, 25, 36, 43], the maximal velocity within the avalanche exceeds the front speed by 30% to 40%. On the quantitative viewpoint, the magnitude of the velocity at a given position of the front seems significantly larger in our simulation than as reported in [21]. In [45], similar discrepancies between (slightly too slow) numerical results and experimental data are attributed to the effect of

numerical diffusion inherent to the used scheme.

Eventually, we perform the same simulation but working with the dimensionless system. To this end, we use as characteristic units the height of the avalanche  $L = h_0 = 0.3\text{ m}$ , the mean value of the velocity of the avalanche front, evaluated from Figure 12,  $U = 3.1\text{ m s}^{-1}$ , and the gravity acceleration  $\|g\| = 9.8\text{ m s}^{-2}$ . Accordingly, we obtain for the Froude number  $\text{Fr} \approx 1.8$ . Then, with the kinematic viscosity  $\bar{\nu} = 5 \times 10^{-4}\text{ m}^2\text{ s}^{-1}$ , the Reynolds number is given by  $\text{Re} \approx 900$ . We point out that these parameters are far less numerically demanding than the parameters used in Section 2.3, because the Reynolds number is smaller and the Froude number is larger. The system (10) is solved on the dimensionless domain  $\Omega_\star = [0, 9] \times [0, 2.67]$ , during the time interval  $0 \leq t_\star \leq 15$  with  $\mu_\star(\rho_\star) = \rho_\star$ . Results are displayed in Figure 13. The correspondence between Figures 12 and 13 shows that the definition of the dimensionless parameters  $\text{Fr}$  and  $\text{Re}$  is clearly relevant. On the other hand, the agreement of the simulations with the experimental data discussed in Section 2.3 makes us confident on the simulation of the interaction with an obstacle.

### 3 Conclusion

In this work we discuss a hierarchy of models, including connection to Eulerian-Lagrangian description, for mixtures flows, which applies to many environmental flows. These models are characterized by diffusive fluxes between the different components of the mixture, which induce new constraints in the PDEs system. We propose a specific numerical scheme to simulate the behavior of such systems. The method is based on a time-splitting approach and a hybrid Finite Volume-Finite Element scheme which have shown their efficiency for non homogeneous incompressible flows. The numerical approach we propose is reliable: the possibility of working on unstructured meshes, and thus of coupling the resolution with mesh refinement strategies, make it well-adapted to follow complex fronts typical of such flows. We apply the scheme to investigate avalanches phenomena; comparison with experimental data and numerical simulations available in the literature demonstrates the skills of the method.

### Acknowledgements

We acknowledge Didier Bresch and Céline Acary-Robert for very fruitful discussions about this work, and for friendly advices on the simulations of avalanches.

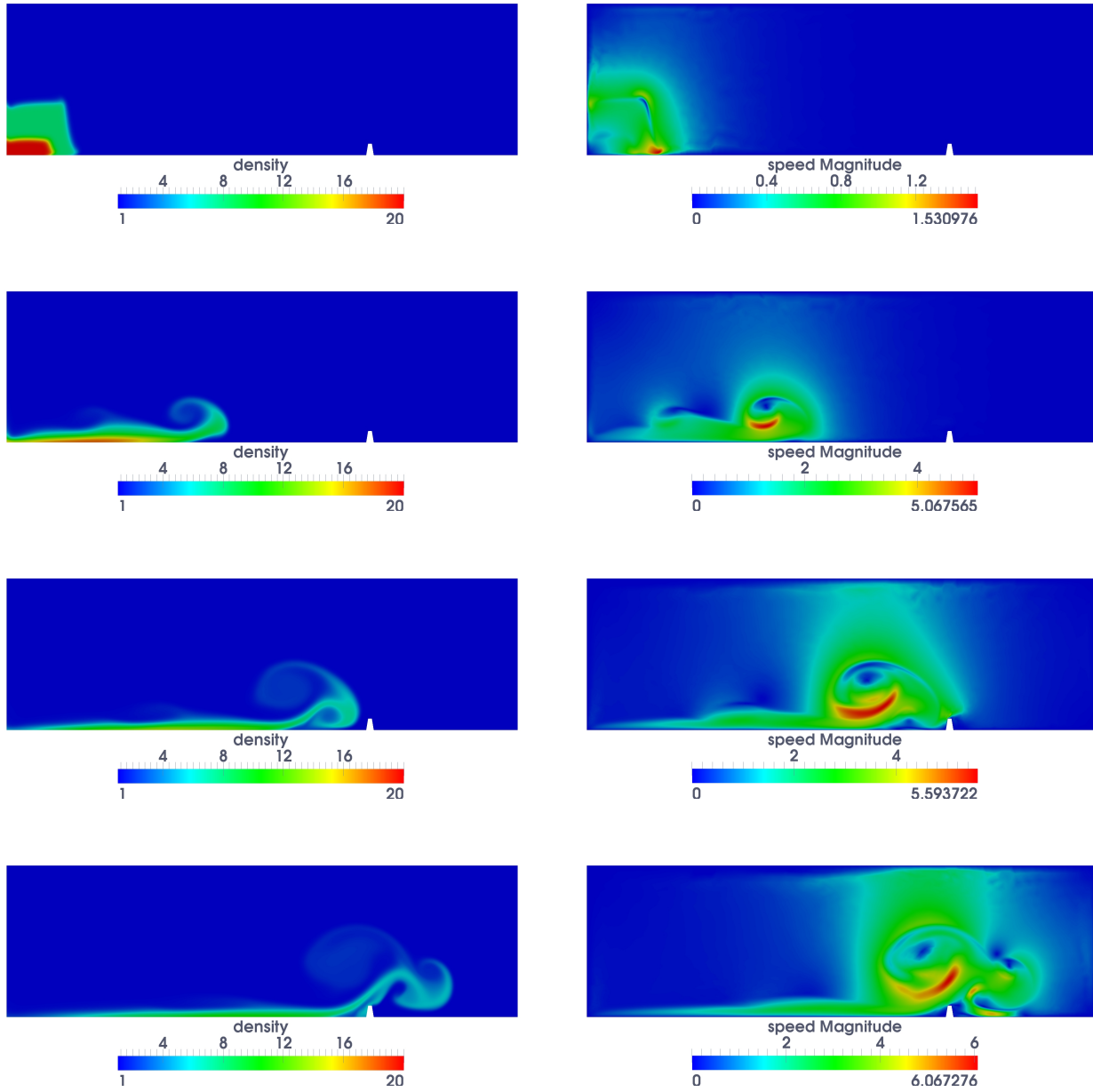


Figure 12: Density (left column) and speed magnitude (right column) at times  $t=0.10$  s,  $0.50$  s,  $0.80$  s and  $1.00$  s (from top to bottom).

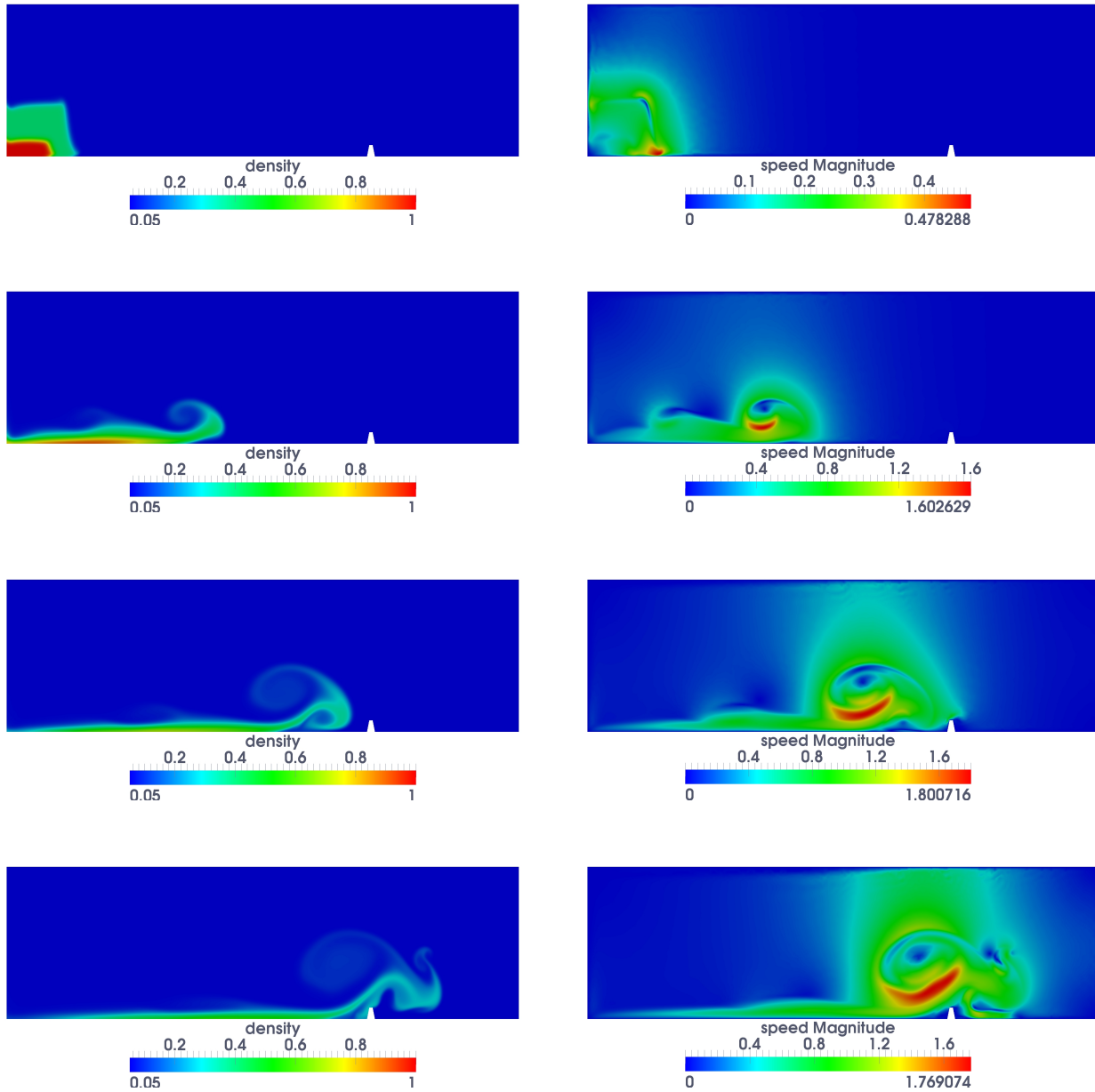


Figure 13: Dimensionless density (left column) and speed magnitude (right column) at times  $t_* = 1.03, 5.16, 8.26, 10.33$  (corresponding to  $t=0.10$  s,  $0.50$  s,  $0.80$  s and  $1.00$  s) (from top to bottom), using the dimensionless form of the equations, with  $Fr = 1.8$  and  $Re = 900$ .

# A A derivation from the Eulerian–Lagrangian modeling

We propose in this Appendix a possible derivation of the constraint (3) starting from a Eulerian–Lagrangian description of the mixture.

## A.1 Introduction to the model

In this Section the disperse phase is thought of as a large set of droplets (for instance it can be applied to aerosols powder-snow avalanches). This description involves a coupling between the mass and momentum conservation for the fields  $(\rho_f, u_f)$  characterizing the fluid and a kinetic equation satisfied by the particle distribution function  $F(t, x, \xi)$  describing the dilute phase. In other words, the dilute phase is seen as a set of disperse particles for which we adopt a statistical viewpoint:  $F(t, x, \xi) d\xi dx$  corresponds to the probability of finding particles of the disperse phase having at time  $t$  their position and velocity in the infinitesimal domain centered at  $(x, \xi)$  with volume  $d\xi dx$ . (Up to a suitable rescaling it can be thought of equivalently as the number of particles occupying the infinitesimal domain of the phase space.) This modeling applies for particles suspension where a typical measure of the size of the particles is small compared to the interparticles distance. From now on, we discuss the modeling issues considering the natural three-dimensional framework. Assuming that particles are spherically shaped with radius  $a > 0$ ,

$$\phi(t, x) = \frac{4}{3}\pi a^3 \int_{\mathbb{R}^3} F(t, x, \xi) d\xi$$

is interpreted as the volume fraction occupied by the particles. We define accordingly the mass density and momentum of the disperse phase

$$\rho_d(t, x) = \bar{\rho}_d \phi(t, x), \quad \rho_d u_d(t, x) = \bar{\rho}_d \phi u_d(t, x) = \frac{4}{3}\pi a^3 \bar{\rho}_d \int_{\mathbb{R}^3} \xi F(t, x, \xi) d\xi.$$

The system of PDEs describing the behavior of the mixture reads as follows. First, we write the mass and momentum conservation equation for the dense phase, namely

$$\partial_t \rho_f + \nabla_x \cdot (\rho_f u_f) = 0, \tag{15}$$

$$\partial_t (\rho_f u_f) + \text{Div}_x (\rho_f u_f \otimes u_f) + \nabla_x p = \rho_f g + \text{Div}_x (\mu \mathbb{D}(u_f)) + \text{Drag}_f$$

where the last term in the momentum equation accounts for the drag force exerted by the particles on the fluid. The particle distribution function  $F(t, x, \xi)$  obeys

$$\partial_t F + \xi \cdot \nabla_x F + \left(1 - \frac{\bar{\rho}_f}{\bar{\rho}_d}\right) g \cdot \nabla_\xi F = \nabla_\xi \cdot \left(-\text{Drag}_d F + D \nabla_\xi F\right). \tag{16}$$

In this equation we take into account gravity/buoyancy effects on the particles that gives rise to the acceleration term  $(1 - \bar{\rho}_f/\bar{\rho}_d)g \cdot \nabla_\xi F$ , with  $g$  the gravitational acceleration. The right hand

side in (16) describes both the drag force exerted by the fluid on the particles and the Brownian motion of the particles. Brownian motion induces diffusion with respect to the velocity variable, with a diffusion coefficient defined by the following Einstein formula [22]

$$D = \frac{9\mu}{2\bar{\rho}_d a^2} \frac{3k\theta}{4\pi a^3 \bar{\rho}_d},$$

where  $\mu$  is the dynamic viscosity of the fluid,  $\theta$  is the temperature of the flow, assumed a fixed positive constant and  $k$  stands for the Boltzmann constant. The expression of the drag force can be a quite intricate and non linear function, derived from phenomenological considerations and depending on the densities  $\rho_f$ ,  $\rho_d$ , the viscosity  $\mu$ , the radius  $a$  and the relative velocity  $\xi - u$ . Here we restrict ourselves to the situation where it is given by the Stokes law, hence a linear function of the relative velocity

$$-\text{Drag}_d = \frac{9\mu}{2a^2 \bar{\rho}_d} Z(\phi) (\xi - u_f)$$

with a certain (dimensionless) function  $Z : [0, \infty) \rightarrow [0, \infty)$ . Note that the viscosity itself might be a function of the volume fraction  $\phi$ . The right hand side in (16) then becomes

$$\frac{9\mu}{2a^2 \bar{\rho}_d} \nabla_\xi \cdot \left( Z(\phi) (\xi - u_f) F + \frac{3k\theta}{4\pi a^3 \bar{\rho}_d} \nabla_\xi F \right).$$

We refer for instance to [22] or more recently [31] for a thorough discussion on this Fokker–Planck operator. The drag force exerted on the fluid by the particles is the back–reaction to the drag force exerted by the fluid on the particles. Hence, taking into account all particles located at position  $x$  it is defined by the velocity average

$$\text{Drag}_f = -\frac{4}{3} \pi a^3 \bar{\rho}_d \int_{\mathbb{R}^3} \text{Drag}_d F \, d\xi.$$

(Note that with our convention  $\text{Drag}_d$  is homogeneous to  $\frac{\text{Velocity}}{\text{Time}}$ , while  $\text{Drag}_f$  is homogeneous to  $\frac{\text{Mass} \times \text{Velocity}}{\text{Volume} \times \text{Time}}$ .) As a matter of fact, we can write

$$\text{Drag}_f = 6\pi\mu a Z(\phi) \int_{\mathbb{R}^3} (\xi - u_f) F \, d\xi = \frac{9\mu}{2a^2 \bar{\rho}_d} Z(\phi) \rho_d (u_d - u_f).$$

The model is closed by setting

$$\rho_f(t, x) = \bar{\rho}_f (1 - \phi(t, x)).$$

In other words, we assume here that the fluid is incompressible in the sense that the mass density remains constant in the domain occupied by the dense phase; nevertheless we account locally for

the volume occupied by the particles in the mass and momentum balance. Observe that  $\phi(t, x) \geq 0$  but there is no reason guaranteeing that  $\phi$  remains bounded by 1 (except in the case where  $u_f$  is divergence-free: then the first equation in (15) can be rewritten equivalently in non-conservative form, which implies the maximum principle for  $\phi$ ). It as to be considered as a modeling assumption: the equations make sense as far as  $\phi$  remains far below 1, which means that the particles are highly dilute. Naturally, we can define the mass density of the mixture by

$$\rho(t, x) = \rho_f(t, x) + \rho_d(t, x) = \bar{\rho}_f(1 - \phi(t, x)) + \bar{\rho}_d\phi(t, x)$$

and the mean mass velocity is

$$\rho u(t, x) = \rho_f u_f(t, x) + \rho_d u_d(t, x) = \bar{\rho}_f(1 - \phi(t, x))u_f(t, x) + \frac{4}{3}\pi a^3 \bar{\rho}_d \int_{\mathbb{R}^3} \xi F(t, x, \xi) d\xi.$$

Integrating (16) over the velocity variable we obtain

$$\frac{4}{3}\pi a^3 \bar{\rho}_d \left( \partial_t \int_{\mathbb{R}^3} F d\xi + \nabla_x \cdot \int_{\mathbb{R}^3} \xi F d\xi \right) = 0 = \partial_t \rho_d + \nabla_x \cdot (\rho_d u_d)$$

and, similarly, multiplying (16) by  $\xi$  and integrating over the velocity variable, we are led to

$$\begin{aligned} \frac{4}{3}\pi a^3 \bar{\rho}_d & \left( \partial_t \int_{\mathbb{R}^3} \xi F d\xi + \text{Div}_x \int_{\mathbb{R}^3} \xi \otimes \xi F d\xi - \left(1 - \frac{\bar{\rho}_f}{\bar{\rho}_d}\right) g \int_{\mathbb{R}^3} F d\xi \right) \\ & = -6\pi\mu a Z(\phi) \int_{\mathbb{R}^3} (\xi - u_f) F d\xi = -\frac{9\mu}{2a^2 \bar{\rho}_d} Z(\phi) \rho_d (u_d - u_f) \\ & = \partial_t (\rho_d u_d) + \text{Div}_x \left( \frac{4}{3}\pi a^3 \bar{\rho}_d \int_{\mathbb{R}^3} \xi \otimes \xi F d\xi \right) - \left(1 - \frac{\bar{\rho}_f}{\bar{\rho}_d}\right) g \rho_d. \end{aligned}$$

As a matter of fact, combining these relations with (15), we deduce that

$$\begin{aligned} \partial_t \rho + \nabla_x \cdot (\rho u) & = 0, \\ \partial_t (\rho u) + \text{Div}_x \left( \rho_f u_f \otimes u_f + \frac{4}{3}\pi a^3 \bar{\rho}_d \int_{\mathbb{R}^3} \xi \otimes \xi F d\xi \right) + \nabla_x p & = \rho_f g + (\bar{\rho}_d - \bar{\rho}_f) \phi g + \text{Div}_x (\mu \mathbb{D}(u_f)) \end{aligned}$$

holds, that can be interpreted as the total mass conservation and the balance law for the total momentum, respectively. Furthermore, we have

$$\partial_t \left( \frac{\rho_f}{\bar{\rho}_f} + \frac{\rho_d}{\bar{\rho}_d} \right) = \partial_t (1 - \phi + \phi) = 0 = -\nabla_x \cdot \left( \frac{\rho_f}{\bar{\rho}_f} u_f + \frac{\rho_d}{\bar{\rho}_d} u_d \right) = -\nabla_x \cdot ((1 - \phi)u_f + \phi u_d).$$

It recasts as a constraint on the velocity field

$$\nabla_x \cdot ((1 - \phi)u_f) = -\frac{4}{3}\pi a^3 \nabla_x \cdot \int_{\mathbb{R}^3} \xi F d\xi = -\nabla_x \cdot (\phi u_d).$$

We refer for further details on these Eulerian-Lagrangian models to [3, 47, 46, 52]; they are widely used to describe natural or industrial flows like sedimenting and fluidized suspensions, hydraulic fracturing of reservoirs, the dispersion of atmospheric pollutants and dusts...

## B Dimensionless equations and hydrodynamic regimes

We wish to derive a hydrodynamic model with the constraint (3) through asymptotic arguments. To this end, we need to make dimensionless parameters appear:

- We introduce time and length scales of reference, say  $T$  and  $L$ , and we set  $U = L/T$  as the velocity unit.
- We define the thermal velocity as to be  $V_{th} = \sqrt{\frac{3k\theta}{4\pi a^3 \bar{\rho}_d}}$ .
- We introduce a typical value  $0 < \bar{\phi} < 1$  of the particle volume fraction (in practice the quantity is quite small compared to 1), and a typical value of the viscosity  $\bar{\mu}$ .
- The driving parameters defined by means of the physical properties of the constituents are the Stokes settling time  $\frac{2\bar{\rho}_d a^2}{9\bar{\mu}}$ , and the ratio of the mass densities  $\frac{\bar{\rho}_d}{\bar{\rho}_f}$ . We set

$$\epsilon = \frac{2\bar{\rho}_d a^2}{9\bar{\mu}T}, \quad \eta = \frac{V_{th}}{U}, \quad \bar{g} = g \frac{T^2}{L}$$

- We define dimensionless variables and unknowns as follows

$$\begin{aligned} t &= Tt_*, & x &= Lx_*, & v &= V_{th}v_*, \\ F(t, x, v) &= \frac{3}{4\pi a^3} \frac{1}{V_{th}^3} \bar{\phi} F_*(t_*, x_*, v_*), \\ \phi(t, x) &= \bar{\phi} \phi_*(t_*, x_*) = \bar{\phi} \int_{\mathbb{R}^3} F(t_*, x_*, v_*) dv_*, \\ \rho_{f*} &= (1 - \bar{\phi}\phi_*), & u_f(t, x) &= U u_{f*}(t_*, x_*), \\ \mu &= \bar{\mu} \mu_*(\phi_*), & Z &= Z_*(\phi_*). \end{aligned}$$

Endowed with these definitions, we are led to

$$\begin{aligned} \partial_{t_*} F_* + \eta \xi_* \cdot \nabla_{x_*} F_* + \left(1 - \frac{\bar{\rho}_f}{\bar{\rho}_d}\right) \frac{\bar{g}}{\eta} \cdot \nabla_{\xi_*} F_* &= \frac{\mu_*(\phi_*)}{\epsilon} \nabla_{\xi_*} \cdot (Z_*(\phi_*) (\xi_* - u_{f*}/\eta) F_* + \nabla_{\xi_*} F_*), \\ \partial_{t_*} \rho_{f*} + \nabla_{x_*} \cdot (\rho_{f*} u_{f*}) &= 0, \\ \partial_{t_*} (\rho_{f*} u_{f*}) + \text{Div}_{x_*} (\rho_{f*} u_{f*} \otimes u_{f*}) + \nabla_{x_*} p_* & \\ &= \text{Div}_{x_*} (\mu_* \mathbb{D}(u_{f*})) + \rho_{f*} \bar{g} + \frac{\bar{\phi} \bar{\rho}_d}{\epsilon \bar{\rho}_f} \mu_*(\phi_*) Z_*(\phi_*) \int_{\mathbb{R}^3} (\eta \xi_* - u_{f*}) F_* d\xi_*. \end{aligned}$$

For the sake of simplicity, we have assumed that the units are such that the diffusion coefficient scales as  $\frac{\bar{\mu}T}{\bar{\rho}_f L^2} = 1$ . We are interested in regimes where  $0 < \epsilon \ll 1$ . It leads to relaxation processes since the particle distribution function is pushed to resemble a Maxwellian. This is reminiscent

of hydrodynamic regimes in gas dynamics [49]. Indeed, the penalization of the Fokker–Planck operator drives  $F_\star$  towards an element of the kernel of this operator:

$$F_\star \simeq \mathcal{M}_\star, \quad \nabla_{\xi_\star} \cdot (Z_\star(\phi_\star) (\xi_\star - u_{f_\star}/\eta)\mathcal{M}_\star + \nabla_{\xi_\star}\mathcal{M}_\star) = 0,$$

which eventually means

$$\begin{aligned} F_\star(t_\star, x_\star, \xi_\star) &\simeq \mathcal{M}_\star(t_\star, x_\star, \xi_\star) \\ &\simeq \phi_\star(t_\star, x_\star) \left( \frac{Z_\star(\phi_\star(t_\star, x_\star))}{2\pi} \right)^{3/2} \exp\left( - \frac{Z_\star(\phi_\star(t_\star, x_\star)) |\xi_\star - u_{f_\star}(t_\star, x_\star)/\eta|^2}{2} \right). \end{aligned}$$

However, the details of the asymptotics depends on the behavior of the other scaling parameters with respect to  $\epsilon$ , which will be discussed in a while. In order to investigate the asymptotic behavior as  $\epsilon$  tends to 0, it is convenient to introduce the following notation

$$\begin{pmatrix} \phi_\star \\ J_\star \\ \mathbb{P}_\star \end{pmatrix} = \int_{\mathbb{R}^3} \begin{pmatrix} 1 \\ \eta\xi \\ \xi \otimes \xi \end{pmatrix} F_\star d\xi.$$

The moment equations now recast as follows

$$\begin{aligned} \partial_{t_\star}\phi_\star + \nabla_{x_\star} \cdot J_\star &= 0, \\ \partial_{t_\star}J_\star + \eta^2 \text{Div}_{x_\star}\mathbb{P}_\star - \left(1 - \frac{\bar{\rho}_f}{\bar{\rho}_d}\right)\bar{g}\phi_\star &= -\frac{\mu_\star(\phi_\star)Z_\star(\phi_\star)}{\epsilon}(J_\star - \phi_\star u_{f_\star}). \end{aligned} \quad (17)$$

Of course, these relations are nothing but the dimensionless version of the evolution equations derived above for  $\rho_d$  and  $\rho_d u_d$ . Note that the system is not closed since the higher moment  $\mathbb{P}_\star$  cannot be expressed in general by means of  $\phi_\star$  and  $J_\star$ . The equation for the fluid velocity becomes

$$\partial_{t_\star}(\rho_{f_\star} u_{f_\star}) + \text{Div}_{x_\star}(\rho_{f_\star} u_{f_\star} \otimes u_{f_\star}) + \nabla_{x_\star} p_\star = \text{Div}_{x_\star}(\mu_\star \mathbb{D}(u_{f_\star})) + \rho_{f_\star} \bar{g} + \frac{\bar{\phi} \bar{\rho}_d}{\epsilon \bar{\rho}_f} \mu_\star(\phi_\star) Z_\star(\phi_\star) (J_\star - \phi_\star u_{f_\star}).$$

In rescaled form the mean density of the mixture reads

$$\rho_\star = \rho_{f_\star} + \bar{\phi} \frac{\bar{\rho}_d}{\bar{\rho}_f} \phi_\star$$

while the velocity of the mixture is defined by

$$\rho_\star u_\star = \rho_{f_\star} u_{f_\star} + \bar{\phi} \frac{\bar{\rho}_d}{\bar{\rho}_f} J_\star.$$

Therefore, we are led to

$$\begin{aligned} \partial_{t_\star} \rho_\star + \nabla_{x_\star} \cdot (\rho_\star u_\star) &= 0, \\ \partial_{t_\star} (\rho_\star u_\star) + \text{Div}_{x_\star} \left( \rho_{f_\star} u_{f_\star} \otimes u_{f_\star} + \bar{\phi} \frac{\bar{\rho}_d}{\bar{\rho}_f} \eta^2 \mathbb{P}_\star + \nabla_{x_\star} p_\star \right) &= \text{Div}_{x_\star} (\mu_\star \mathbb{D}(u_{f_\star})) + \bar{g} \left( \rho_{f_\star} + \bar{\phi} \left( \frac{\bar{\rho}_d}{\bar{\rho}_f} - 1 \right) \phi_\star \right). \end{aligned}$$

In order to make diffusion effects appear in the evolution of the particles volume fraction, it is necessary to introduce the following scaling assumption

$$0 < \epsilon \ll 1, \quad \bar{\phi} \frac{\bar{\rho}_d}{\bar{\rho}_f} \frac{1}{\epsilon} = \bar{\phi} \frac{\bar{\rho}_d}{\bar{\rho}_f} \eta^2 = 1$$

or, in other words

$$\eta = \frac{1}{\sqrt{\epsilon}} \gg 1, \quad \bar{\phi} \frac{\bar{\rho}_d}{\bar{\rho}_f} = \epsilon \ll 1.$$

(In fact  $\frac{\bar{\phi}}{\epsilon} \frac{\bar{\rho}_d}{\bar{\rho}_f}$  and  $\bar{\phi} \frac{\bar{\rho}_d}{\bar{\rho}_f} \eta^2$  can be assumed to tend to any positive constants, the important fact being to impose the behavior with respect to  $\epsilon$ .) Therefore, combining the relaxation effect induced by making the Fokker–Planck operator stiff to the velocity scaling, we expect as  $\epsilon$  goes to 0 that the particles distribution function looks like a centered Maxwellian

$$F_\star \simeq \frac{\phi_\star}{(2\pi/Z_\star(\phi_\star))^{3/2}} e^{-Z_\star(\phi_\star)|\xi_\star|^2/2}.$$

Accordingly the kinetic pressure becomes

$$\mathbb{P}_\star = \int_{\mathbb{R}^3} \xi \otimes \xi F_\star d\xi_\star \simeq \frac{\phi_\star}{Z_\star(\phi_\star)} \mathbb{I}.$$

Taking into account the scaling assumption, the evolution of the first order moment is governed by

$$\epsilon \partial_{t_\star} J_\star + \text{Div}_{x_\star} \mathbb{P}_\star - \epsilon \bar{g} \left(1 - \frac{\bar{\rho}_f}{\bar{\rho}_d}\right) \phi_\star = -\mu_\star(\phi_\star) Z_\star(\phi_\star) (J_\star - \phi_\star u_{f_\star}).$$

Let us suppose that

$$\epsilon \left(1 - \frac{\bar{\rho}_f}{\bar{\rho}_d}\right) \rightarrow \kappa \in \mathbb{R}.$$

The sign of  $\kappa$  determines whether particles are dominated by gravity ( $\kappa > 0$ ) or buoyancy ( $\kappa < 0$ ). To describe the asymptotic behavior, we assume that the sequences of unknowns admit limit

$$\phi_\star, J_\star, u_{f_\star} \rightarrow \Phi_\ell, J_\ell, u_\ell$$

in a strong enough sense so that we can pass to the limit in non linearities. We bear in mind that  $\bar{\phi}$  remains a free scaling parameter; we assume that  $\bar{\phi} \rightarrow \bar{\phi}_\ell$ . Then, letting  $\epsilon$  go to 0, we arrive at

$$\begin{aligned} \partial_{t_\star} \Phi_\ell + \nabla_{x_\star} \cdot J_\ell &= 0, \\ \nabla_{x_\star} \left( \frac{\Phi_\ell}{Z_\star(\Phi_\ell)} \right) - \kappa \bar{g} \Phi_\ell &= -\mu_\star(\Phi_\ell) Z_\star(\Phi_\ell) (J_\ell - \Phi_\ell u_\ell). \end{aligned}$$

Hence  $\Phi_\ell$  is solution of a nonlinear convection–diffusion equation

$$\partial_{t_\star} \Phi_\ell + \nabla_{x_\star} \cdot \left( \Phi_\ell u_\ell + \frac{1}{\mu_\star(\Phi_\ell) Z_\star(\Phi_\ell)} \left( \kappa \bar{g} \Phi_\ell - \nabla_{x_\star} \frac{\Phi_\ell}{Z_\star(\Phi_\ell)} \right) \right) = 0.$$

Now, the mean density reads  $\rho_\star = (1 - \bar{\phi} \phi_\star) + \epsilon \phi_\star \rightarrow \rho_\ell = (1 - \bar{\phi}_\ell \Phi_\ell)$  and the mean velocity satisfies  $\rho_\star u_\star = (1 - \bar{\phi} \phi_\star) u_{f_\star} + \epsilon J_\star \rightarrow \rho_\ell u_\ell$ . Then, the momentum equation becomes

$$\partial_{t_\star} (\rho_\ell u_\ell) + \text{Div}_{x_\star} (\rho_\ell u_\ell \otimes u_\ell) + \nabla_x \left( p_\ell + \frac{\Phi_\ell}{Z_\star(\Phi_\ell)} \right) = \text{Div}_{x_\star} (\mu_\star \mathbb{D}(u_\ell)) + \bar{g} (\rho_\ell + \kappa \Phi_\ell).$$

For the last term, we have used the equality  $\bar{g} \bar{\phi} \left( \frac{\bar{\rho}_d}{\bar{\rho}_f} - 1 \right) \phi_\star = \bar{g} \bar{\phi} \frac{\bar{\rho}_d}{\bar{\rho}_f} \frac{1}{\epsilon} \epsilon (1 - \frac{\bar{\rho}_f}{\bar{\rho}_d}) \phi_\star = \bar{g} \epsilon (1 - \frac{\bar{\rho}_f}{\bar{\rho}_d}) \phi_\star \rightarrow \bar{g} \kappa \Phi_\ell$ . The mass conservation reads

$$\begin{aligned} \partial_{t_\star} \rho_\ell + \nabla_{x_\star} \cdot (\rho_\ell u_\ell) &= 0 \\ &= -\bar{\phi}_\ell (\partial_t \Phi_\ell + \nabla_{x_\star} \cdot (\Phi_\ell u_\ell)) + \nabla_{x_\star} \cdot u_\ell = 0. \end{aligned}$$

Then, we distinguish two situations:

- Either  $\bar{\phi}_\ell = 0$ , and thus  $\rho_\ell = 1$ ; in such a case the velocity is merely divergence free  $\nabla_{x_\star} \cdot u_\ell = 0$ ,
- Or  $\bar{\phi}_\ell > 0$ : in such a case the velocity field is required to satisfy the constraint

$$\nabla_{x_\star} \cdot u_\ell = \bar{\phi}_\ell \nabla_{x_\star} \cdot \left( \frac{1}{\mu_\star(\Phi_\ell) Z_\star(\Phi_\ell)} \left( \nabla_{x_\star} \frac{\Phi_\ell}{Z_\star(\Phi_\ell)} - \kappa \bar{g} \Phi_\ell \right) \right).$$

Further mathematical analysis of the asymptotics is beyond the scope of the present paper. We refer to [32, 33] for technical details on such questions.

**Example 1** *A relevant situation corresponds to the case where we use the Einstein definition of the effective viscosity of the solution, see [23, 7]*

$$\mu(\phi) = \bar{\mu} \times \left( 1 + \frac{5}{2} \phi \right).$$

Assuming  $Z = 1$ ,  $\bar{g} = 0$ , it yields

$$\nabla_{x_\star} \cdot u_\ell = \frac{2}{5} \Delta_{x_\star} \ln \left( 1 + \frac{5}{2} \bar{\phi} \Phi_\ell \right) = -\frac{2}{5} \Delta_{x_\star} \ln \left( \frac{7}{2} - \frac{5}{2} \rho_\ell \right).$$

*A relevant generalization of this simple law for the effective viscosity is proposed e. g. in [15]. Using the Stokes law for the drag force makes sense when the particle Reynolds number  $\frac{2\rho_f |u_f - V_{th}| a}{\mu}$  is small. The simplest case with  $Z = 1$  is used in many applications, see for instance [39, 42]. More complex examples have the form  $Z(\phi) = (1 - \phi)^{-\kappa}$ , see [47,  $\kappa = 2.8$  in Eq. (7)], [3,  $\kappa = 2.65$  in Eq. (5)] or [44].*

## References

- [1] T. Alazard. Low Mach number flows and combustion. *SIAM J. Math. Anal.*, 38:1186–1213, 2006.
- [2] T. Alazard. A minicourse on the low Mach number limit. *Discrete and Continuous Dynamical Systems-Series S*, 3:365–404, 2008.
- [3] M. J. Andrews and P. J. O’Rourke. The multiphase particle-in-cell (MP-PIC) method for dense particulate flows. *Int. J. Multiphase Flow*, 22(2):379–402, 1996.
- [4] G. Ansanay-Alex. *Un schéma éléments finis non-conformes/volumes finis pour l’approximation en maillages non structurés des écoulements à faible nombre de Mach*. PhD thesis, Université de Provence, Aix-Marseille, France, 2009.
- [5] S. N. Antontsev, A. V. Kazhikhov, and V. N. Monakhov. *Boundary value problems in mechanics of nonhomogeneous fluids*, volume 22 of *Studies in Math. and its Appl.* North Holland, 1990.
- [6] H. Beirao da Veiga. Diffusion on viscous fluids. Existence and asymptotic properties of solutions. *Annali Scuola Norm. Sup. Pisa, Classe di Scienze*, 10:341–355, 1983.
- [7] J. F. Brady. The Einstein viscosity correction in  $n$  dimensions. *Int. J. Multiphase Flow*, 10(1):113–114, 1983.
- [8] H. Brenner. Unsolved problems in fluid mechanics: On the historical misconception of fluid velocity as mass motion, rather than volume motion, 2003. Communication for the 100th anniversary of the Ohio State Chemical Engineering Department.
- [9] H. Brenner. Navier-Stokes revisited. *Phys. A*, 349(1-2):60–132, 2005.
- [10] H. Brenner. Bi-velocity hydrodynamics: multicomponent fluids. *Internat. J. Engrg. Sci.*, 47:902–929, 2009.
- [11] H. Brenner. Diffuse volume transport in fluids. *Phys. A*, 389:4026–4045, 2010.
- [12] D. Bresch, El H. Essoufi, and M. Sy. Effect of density dependent viscosities on multiphase incompressible fluid models. *J. Math. Fluid Mech.*, 9(3):377–397, 2007.
- [13] C. Calgaro, E. Chane-Kane, E. Creusé, and T. Goudon.  $L^\infty$  stability of vertex-based MUSCL finite volume schemes on unstructured grids; simulation of incompressible flows with high density ratios. *J. Comput. Phys.*, 229(17):6027–6046, 2010.

- [14] C. Calgaro, E. Creusé, and T. Goudon. An hybrid finite volume-finite element method for variable density incompressible flows. *J. Comput. Phys.*, 227(9):4671–4696, 2008.
- [15] N. S. Cheng and A. W. K. Law. Exponential formula for computing effective viscosity. *Powder Technology*, 129(1-3):156–160, 2003.
- [16] M. Clément-Rastello. *Etude de la dynamique des avalanches de neige en aérosol*. PhD thesis, Univ. Joseph Fourier, Grenoble, 2002.
- [17] R. Danchin. Density-dependent incompressible fluids in bounded domains. *J. Math. Fluid Mech.*, 2005.
- [18] C. Debiez, A. Dervieux, K. Mer, and B. Nkonga. Computation of unsteady flows with mixed finite volume/finite element upwind methods. *Internat. J. Numer. Methods Fluids*, 27(1-4, Special Issue):193–206, 1998.
- [19] B. Desjardins. Global existence results for the incompressible density-dependent Navier-Stokes equations in the whole space. *Differential and Integral Equations*, 10:587–598, 1997.
- [20] J. Droniou and C. Le Potier. Construction and convergence study of schemes preserving the elliptic local maximum principle. *SIAM J. Numer. Anal.*, 49(2):459–490, 2011.
- [21] D. Dutykh, C. Acary-Robert, and D. Bresch. Mathematical modeling of powder-snow avalanche flows. *Stud. Appl. Math.*, 127(1):38–66, 2011.
- [22] A. Einstein. On the motion of small particles suspended in liquids at rest required by the molecular-kinetic theory of heat. *Ann. Physik*, 17:549–560, 1905.
- [23] A. Einstein. Eine neue bestimmung der moleküldimensionen. *Ann. Physik*, 19:289–306, 1906. Doctoral dissertation, Zurich, 1905.
- [24] J. Etienne. *Simulation numérique directe de nuages aérosols denses sur des pentes ; application aux avalanches de neige poudreuse*. PhD thesis, Institut National Polytechnique de Grenoble, 2004.
- [25] J. Etienne, P. Saramito, and E.J. Hopfinger. Numerical simulations of dense clouds on steep slopes : Application to powder-snow avalanches. *Ann. Glaciol.*, 38:379–383(5), 2004. Presented at IGS International Symposium on Snow and Avalanches. Davos, Switzerland 2-6 June 2003.
- [26] R. E. Ewing, T. Lin, and Y. Lin. On the accuracy of the finite volume element method based on piecewise linear polynomials. *SIAM J. Num. Anal.*, 39(6):1865–1888, 2002.
- [27] R. Eymard, T. Gallouët, and R. Herbin. Finite volume methods. In *Handbook of numerical analysis, Vol. VII*, Handb. Numer. Anal., VII, pages 713–1020. North-Holland, Amsterdam, 2000.

- [28] R. Eymard, D. Hilhorst, and M. Vohralík. A combined finite volume-finite element scheme for the discretization of strongly nonlinear convection-diffusion-reaction problems on nonmatching grids. *Numer. Methods Partial Differential Equations*, 26(3):612–646, 2010.
- [29] E. Feireisl and A. Vasseur. New perspectives in fluid dynamics: Mathematical analysis of a model proposed by Howard Brenner. Technical report, University of Texas at Austin, 2010.
- [30] F. Franchi and B. Straughan. A comparison of Graffi and Kazhikov–Smagulov models for top heavy pollution instability. *Adv. in Water Resources*, 24:585–594, 2001.
- [31] V. S. Galkin and S. V. Rusakov. Kinetic Fokker–Planck equation for free-molecular, thermally nonequilibrium Brownian particles in an inhomogeneous gas. *Fluid Dynamics*, 42:330–334, 2007. Originally published in *Izvestiya Rossiiskoi Akademii Nauk, Mekhanika Zhidkosti i Gaza*, 2007, Vol. 42, No. 2, pp. 204–208 (in Russian).
- [32] T. Goudon, P.-E. Jabin, and A. Vasseur. Hydrodynamic limit for the Vlasov-Navier-Stokes equations. I. Light particles regime. *Indiana Univ. Math. J.*, 53(6):1495–1515, 2004.
- [33] T. Goudon, P.-E. Jabin, and A. Vasseur. Hydrodynamic limit for the Vlasov-Navier-Stokes equations. II. Fine particles regime. *Indiana Univ. Math. J.*, 53(6):1517–1536, 2004.
- [34] D. Graffi. Il teorema di unicità per i fluidi incompressibili, perfetti, eterogenei. *Rev. Unione Mat. Argentina*, 17:73–77, 1955.
- [35] F. Guillén-González and J. V. Gutiérrez-Santacreu. Unconditional stability and convergence of fully discrete schemes for  $2d$  viscous fluids models with mass diffusion. *Math. of Comp.*, 77(263):1495–1524, 2008.
- [36] K. Hutter and R. Greve. Two-dimensional similarity solutions for finite-mass granular avalanches with Coulomb and viscous-type frictional resistance. *J. Glaciol.*, 39:357–372, 1993.
- [37] D. D. Joseph and Y. Y. Renardy. *Fundamentals of two-fluid dynamics. Part II: Lubricated Transport, Drops and Miscible Liquids*, volume 3 of *Interdisciplinary Applied Mathematics*. Springer-Verlag, New York, 1993. Mathematical theory and applications.
- [38] A. V. Kazhikhov and S. Smagulov. The correctness of boundary value problems in a diffusion model in an inhomogeneous fluid. *Sov. Phys. Dokl.*, 22:249–250, 1977.
- [39] G. Lavergne. Modélisation de l’écoulement multiphasique dans le propulseur à poudre P230 d’Ariane 5. Ile d’Oléron, 2004. Lecture Notes of the School of the Groupement Français de Combustion.

- [40] P.-L. Lions. *Mathematical topics in fluid mechanics. Vol. 1 : Incompressible models*, volume 3 of *Oxford Lecture Series in Mathematics and its Applications*. The Clarendon Press Oxford University Press, New York, 1996. Oxford Science Publications.
- [41] P.-L. Lions. *Mathematical topics in fluid mechanics. Vol. 2 : Compressible models*, volume 10 of *Oxford Lecture Series in Mathematics and its Applications*. The Clarendon Press Oxford University Press, New York, 1998. Oxford Science Publications.
- [42] J. Mathiaud. *Etude de systèmes de type gaz-particules*. PhD thesis, ENS Cachan, 2006.
- [43] F. Naaim-Bouvet. *Approche macro-structurelles des écoulements bi-phasiques turbulents de neige et de leur interaction avec des obstacles*. Habilitation à diriger les recherches, Univ. Joseph Fourier, Grenoble, 2003.
- [44] P. J. O'Rourke. *Collective drop effects on vaporizing liquid sprays*. PhD thesis, Princeton University, NJ, 1981.
- [45] S. Pain. Simulation numérique de l'interaction entre une avalanche en aérosol et une digue d'arrêt. *Publication interne ENGEES/CEMAGREF*, 2002.
- [46] N. A. Patankar and D. D. Joseph. Lagrangian numerical simulation of particulate flows. *Int. J. Multiphase Flow*, 27:1685–1706, 2001.
- [47] N. A. Patankar and D. D. Joseph. Modeling and numerical simulation of particulate flows by the Eulerian–Lagrangian approach. *Int. J. Multiphase Flow*, 27:1659–1684, 2001.
- [48] K. R. Rajagopal and L. Tao. *Mechanics of mixtures*, volume 35 of *Series on Advances in Math. for Appl. Sci.* World Scientific, 1985.
- [49] L. Saint Raymond. *Hydrodynamic Limits of the Boltzmann Equation*, volume 1971 of *Lect. Notes in Math.* Springer, 2009.
- [50] P. Secchi. On the initial value problem for the equations of motion of viscous incompressible fluids in the presence of diffusion. *Boll. Un. Mat. Ital. B (6)*, 1(3):1117–1130, 1982.
- [51] P. Secchi. On the motion of viscous fluids in the presence of diffusion. *SIAM J. Math. Anal.*, 19(1):22–31, 1988.
- [52] D. M. Snider, P. J. O'Rourke, and M. J. Andrews. Sediment flow in inclined vessels calculated using a multiphase particle-in-cell model for dense particle flows. *Int. J. Multiphase Flow*, 24:1359–1382, 1998.